Thermodynamic analysis of a synergistic integration of solid oxide fuel cell and solar-based chemical looping methane reforming unit for solar energy storage, power production, and

Energy Conversion and Management 302 (2024) 118080

Contents lists available at ScienceDirect

Energy Conversion and Management

journal homepage: www.elsevier.com/locate/enconman

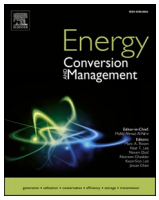

Thermodynamic analysis of a synergistic integration of solid oxide fuel cell and solar-based chemical looping methane reforming unit for solar energy storage, power production, and carbon capture

Salvatore F. Cannone *, Muhammad Ishaq, Andrea Lanzini, Massimo Santarelli

Energy Department (DENERG), Politecnico di Torino, Corso Duca degli Abruzzi 24, 10129 Torino, Italy

A B S T R A C T

This study presents a thermodynamic analysis of a novel concept that synergistically integrates a solid oxide fuel cell with a Ceria-based solar-chemical looping methane reforming system. The integrated configuration aims to simultaneously achieve solar energy storage, electric power production, carbon capture storage, and in situ re-utilization. The proposed hybrid system capitalises on the advantageous features of the solar-chemical looping methane reforming unit, specifically methane reforming and oxygen carrier reduction during the reduction step for solar energy storage, and waste gas dissociation during the oxidation step for energy release. The additional syngas produced is introduced to the fuel cell, enabling further power production and waste stream re-utilization. The schematic process of the system is modelled by solving mass and energy balances at steady-state conditions. The chemical looping parameters (fuel reforming ratio, co-splitting ratio), material parameters (Ceria effectiveness), and fuel cell parameters (temperature, fuel utilisation, operating voltage, and steam-to-carbon ratio) are also examined. The proposed hybrid solar power plant concept exhibits promising characteristics, achieving high electrical and global efficiencies (63.6 % and 70 %, respectively), high energy density (404 kWh/m^3) with partial carbon dioxide re-utilization and net zero emissions.

1. Introduction

Global energy demand is rising sharply and is largely met by fossil fuels. In 2021, the global energy demand increased by 5.4 % compared to the previous year, returning to pre-pandemic levels. Energy-related carbon dioxide (CO_2) emissions have increased globally to 36.6 Gt CO_2 [1]. Considering the various drawbacks of fossil fuel use, effective research and efforts have been made to replace fossil fuels with alternative green energy resources. Among the available renewable energy resources, solar energy is considered one of the most favourable and potential alternatives to fossil fuel-based power plants. Due to its environmentally friendly nature, solar energy is the strongest candidate for the ongoing research and development of plants [2]. However, it is important to acknowledge that despite the progress being made in renewable energy, projections indicate that approximately 80 % of the global energy supply will still rely on fossil fuels by the year 2040. Moreover, natural gas is expected to play a substantial role due to its abundant availability worldwide [3].

Among the various technologies for harnessing solar energy, concentrated solar power (CSP) is seen as a potential option to achieve viable electricity generation. In this technology, solar radiation is concentrated on a receiver and the resulting high temperatures are used to drive a power cycle or endothermic reactions. Although solar power has immense benefits, it is associated with a bottleneck of intermittent supply, which acts as a barrier to achieving economically feasible solutions [5]. To deal with the low energy density, inherently low intensity, and high intermittency of solar power, CSP plants require either an offside backup power generation capability or an onsite storage facility to ensure uninterrupted power generation even when sunlight is no longer available [6].

Solar energy is usually stored in the form of thermal energy storage (TES), which has been developed in three different ways: sensible heat, latent heat and thermochemical energy storage (heat of reaction). Sensible TES uses a temperature increase of the storage medium (water, oil, air, rock, sand, salt) without changing its phase. They have a limited energy density between 60 kWh$_t$/m^3 for sand and 150 kWh$_t$/m^3 for cast iron [7]. Latent TES encompasses a temperature increase in the storage medium, which can be a substance like salt, hydrates, polymers, and so on. Typically, this process also involves a phase transition from a solid state to a liquid phase. This change of phase, such as the melting of a solid into a liquid, is a fundamental characteristic of latent TES systems and is responsible for their ability to store and release energy efficiently. The energy density ranges from 150 kWh$_t$/m^3 to 760 kWh$_t$/m^3 [8]. Thermochemical TES implies an endothermic chemical reaction: the resulting products of this reaction are stored and consumed when solar

* Corresponding author.
E-mail address: salvatore.cannone@polito.it (S.F. Cannone).

https://doi.org/10.1016/j.enconman.2024.118080
Received 1 September 2023; Received in revised form 7 January 2024; Accepted 8 January 2024
Available online 20 January 2024

Nomenclature

A	Area [m2]
AB	Afterburner
ASR	Area Specific Resistance of the cell [O·cm2]
ASU	Air separation unit
C	total current of the stack [A]
CCUS	carbon capture storage and utilization
CL	chemical looping
CLC	chemical looping combustion
CLH	chemical looping hydrogen
CLMR	chemical looping methane reforming
CSP	concentrated solar power
CSR	co-splitting ratio
CYC	cyclone separator
D	diffusion coefficient
DHN	district heating network
DMR	dry methane reforming
DNI	direct normal irradiance [kWh/m2]
F	Faraday constant [C/mol]
f	correction factor
FRR	fuel reforming ratio
FU	fuel utilization
GA	Genetic Algorithm
h	thickness
HEN	heat exchanger network
j	current density in the cell [A/cm2]
LHV	Lower heating value [kWh]
$\dot{n}$	mole flow rate [kmol/hr]
OC	oxygen carrier
P	pressure
Q	Thermal energy [kWh]
R	resistance [Ω]
R	universal gas constant
S/C	steam to carbon ratio [-]
SMR	steam methane reforming
SOFC	solid oxide fuel cell
t	time [hr]
T	temperature
TES	thermal energy storage
U	energy upgrade factor [-]
V	volume
V	voltage [V]
W	Electrical power
WGS	water gas shift
x	molar fraction

Greek letters

δ	non-stochiometric coefficient
η	efficiency
σ	pre-exponential factor [S/cm^2]

Subscripts

red	reduction reactor
oxy	oxydation reactor
sol	solar energy
opt	optical
rec	receiver
ref	reflectivity
clc	clean factor
fld	field
int	interception factor
stor	storage
act	active
an	anode
op	operating
rev	reversal
Kn	knudsen
ely	electrolyte
eff	effective
cat	cathode
ICA	contact loss of anode interconnector [Ωcm^2]
ICC	contact loss of cathode interconnector [Ωcm^2]
aux	auxiliary

energy is not available [7]. Thermochemical TES storage has been extensively studied and recommended by researchers. There are different types of thermochemical storage, ranging from gas-gas or solid–gas storage, where oxidation–reduction reactions take place with an energy density of about 8 kWh/m^3, to storage with carbonate systems that reach an energy density of about 700 kWh/m^3 [9]. In prior research, hybrid thermochemical energy storage systems were explored. These systems were based on the calcium looping (CaL) process, with an integration of solar thermal energy and the investigation of two distinct power cycles, specifically, the Rankine cycle and the supercritical Brayton cycle. The integration of solar CaL with these two cycles resulted in net electrical efficiencies of 39.5 % [10] and 44.4 % [11], respectively.

Chemical looping (CL) is an emerging technology that can be associated with carbon capture utilisation and storage (CCUS) processes [12]. CL is a series of redox (reduction–oxidation) reactions involving oxygen carrier (OC) materials. This process involves the transfer of oxygen (O_2) back and forth between the OC material in various reaction stages. In the reduction step, a high oxidation state material is suitable to be reduced at high temperatures, in a configuration of pure-thermal reduction or of reducing agent-aided reduction configuration. After the reduction step, the reduced material a lower oxidation state [13] is suitable to accept O_2 from other OCs, such as water (H_2O) or CO_2 molecules: the re-oxidation of the solid material provides a thermochemical dissociation of water and/or carbon dioxide, giving hydrogen (H_2) and carbon monoxide (CO), respectively. This CL process is therefore a kind of two-stage thermochemical water/carbon dioxide splitting cycle, as shown in Fig. 1.

Solar thermal energy can drive an endothermic reduction reaction of the CL. One of the first concepts of the solar-fed thermal-driven chemical looping combustion (CLC) process was proposed by Hong and Jin, using methane (CH_4) as the reducing agent and nickel oxide (NiO) as the OC in the reoxidation step [14]. Jafarian et al. explored the issue with a model based on the solar CLC process: NiO is used to convert methane mainly

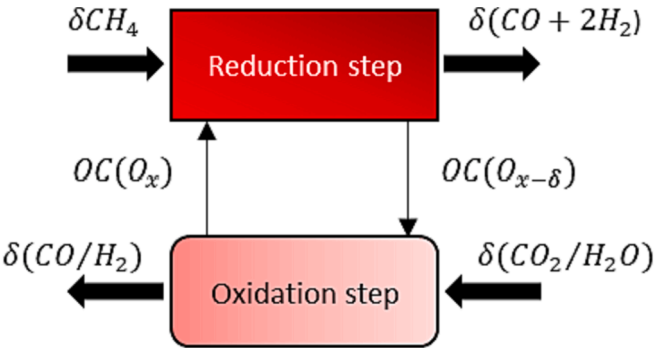

Fig. 1. The simple concept of the two-step chemical looping reforming cycle.

in CO_2 and H_2O, while the reduced OC can be stored; when electricity is required, the reduced material is oxidised in an air reactor, producing air at a very high temperature [15]. Liu et al. have integrated a solar chemical looping hydrogen (CLH) production with a turbine to generate electricity. In the fuel reactor, iron oxide reduction and methane reforming are driven by solar energy. The reformed gas and hydrogen produced during metal oxidation are transferred in a turbine achieving 79 % of system efficiency [16].

Solid oxide fuel cell (SOFC) is an electrochemical machine that converts the chemical energy of fuel into electrical power and is considered one of the most promising options for high-efficiency power generation, with characteristics of fuel flexibility and low carbon emissions. The high operating temperatures of the SOFCs make them versatile in terms of fuel compatibility. These fuel cells can efficiently utilize a wide range of fuels, including liquid hydrocarbons and gaseous fuels. However, direct injection of methane can lead to carbon deposition and a stressful thermal gradient on the anode side. Therefore, the pre-reforming of methane is usually suggested [17].

Chemical looping methane reforming (CLMR) has gained considerable research attention as a promising alternative to conventional CH_4 reforming processes. Its high syngas selectivity, inherent product separation capabilities, and low carbon deposition risk make it an attractive option [18]. Dry methane reforming (DMR) is another approach that co-converts CH_4 and CO_2 into syngas [19]. However, DMR has yet to be commercialized due to challenges such as catalyst instability, carbon deposition, sintering, and high energy consumption. Chemical looping CH_4 conversion coupled with CO_2 utilization offers an alternative solution to conventional pre-reforming unit fed with waste heat from the SOFC. It involves the cyclic circulation of OC between reduction and oxidation environments, enabling efficient product separation, enhanced fuel conversion, reduced carbon deposition, elimination of catalyst regeneration, and mitigating greenhouse gas effect.

CL-integrated SOFC has been investigated by a few authors. A SOFC-based cooling, heating and power system assisted by solar energy (i.e., solar energy is provided to the exhaust gas of a cathode outlet) and integrated CLH production was proposed by Ma et al. [20] which achieved 78 % and 73 % efficiency in cooling and heating mode, respectively. Instead, Spallina et al. proposed a natural gas SOFC plant integrated with CLC to complete the anode exhaust oxidation. With their integration, an electrical efficiency of more than 66 % was evaluated [21].

After conducting a comprehensive literature review, it was observed that there is a noticeable lack of research articles addressing the potential integration of a solar-fed chemical looping process for methane reforming before feeding into a SOFC. This research aims to address this gap by analysing a novel plant concept that combines solar CLMR for solar energy storage with the partial oxidation of methane and the conversion of exhaust gases into syngas. The integrated system also includes an electricity generation plant based on SOFC technology, which eliminates CO_2 emissions and efficiently replaces the need for an external and conventional pre-reformer unit. The main goal of this investigation is to evaluate the attainable system efficiencies of this integrated concept. Additionally, a sensitivity analysis will be conducted

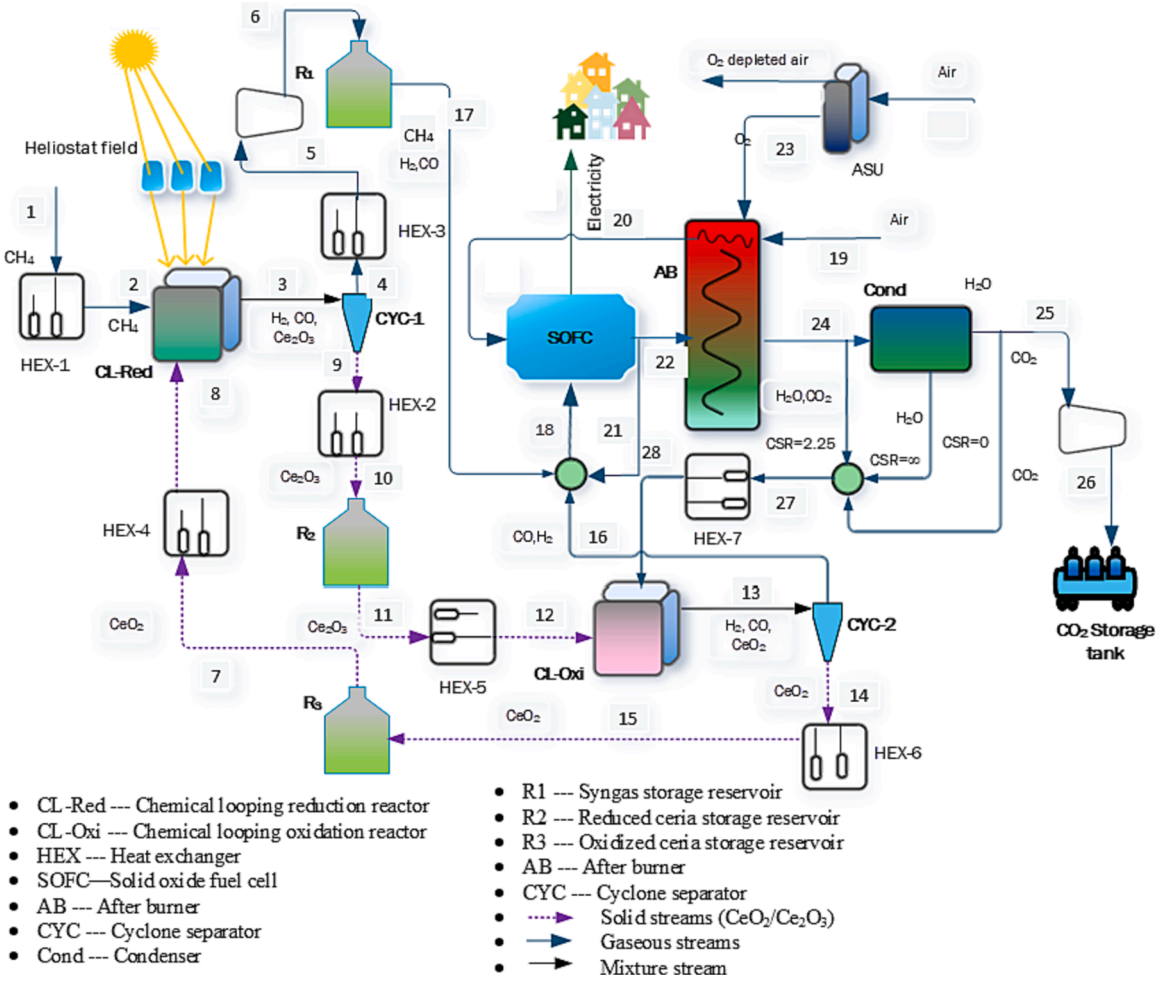

Fig. 2. Conceptional configuration of solar CLMR-SOFC hybrid system assessed to offer the storage of solar thermal energy in the form of chemical energy providing steady state electricity generation. The oxidation reactor is fed with only one stream between: CSR = 2.25 H_2O and CO_2 co-splitting mode; CSR=∞ water splitting mode; CSR = 0 CO_2 splitting mode.

to optimize the system layout and identify key parameters that can enhance overall performance. This research contributes to the field by providing valuable insights into the potential of solar-fed chemical looping methane reforming and its integration with SOFC technology, ultimately advancing the development of efficient and environmentally friendly energy systems.

2. Conceptional design and system description

Fig. 2 shows the simplified configuration and the key components of the proposed solar CLMR-SOFC hybrid system. In this process, the energy required for the partial oxidation of methane and the reduction of OC particles is supplied to the reduction reactor (CL-Red) by CSP. Among various reported metal oxides with redox properties and potentially suitable for thermochemical cycling (e.g., iron oxide [22], cerium (IV) oxide (CeO_2) [23], manganese oxide, copper oxide and cobalt oxide [24]), CeO_2 is selected as the OC. The solar heat from CSP plays a dual role, facilitating the endothermic ceria reduction to cerium (III) oxide Ce_2O_3 and driving the partial oxidation of methane with the oxygen molecules released by ceria. The output of the reduction step is a mixture of reduced ceria and syngas. The reduced ceria particles and syngas are first separated by a cyclone separator (CYC-1), and then cooled and transferred to the syngas reservoir R1 and reduced ceria reservoir R2, respectively.

An SOFC system is proposed to achieve a constant power output. The energy release process consists of a chemical looping oxidation reactor (CL-Oxi), an oxidized ceria reservoir (R3), a cyclone separator (CYC-2), heat exchangers, an SOFC and an afterburner (AB). Ce_2O_3 is released from the storage R2 and oxidized by an exothermic reaction within the oxidation reactor (CL-Oxi). Pure water, pure carbon dioxide or a mixture of these are fed into the oxidation reactor and thermochemically dissociated in the presence of reduced ceria. A mixture of re-oxidized ceria (CeO_2) and hydrogen/carbon monoxide is obtained and separated in the CYC-2 cyclone. The ceria is then transferred to the storage R3, while the reduced gas, the reformed syngas and air are injected into the SOFC to produce heat and electricity.

The exhaust gas from the SOFC consists mainly of H_2O, CO_2, and a small amount of unreacted fuel species (H_2, CO, CH_4). The unprocessed fuel fraction is combusted in the AB utilising pure oxygen supplied by an air separation unit (ASU), thereby converting the residual chemical energy of the SOFC exhaust into thermal energy. Finally, water and carbon dioxide are separated by condensation, and carbon content is captured and sent for storage after being compressed to the required pressure.

3. Methods and equations

The modelling of the proposed solar CLMR-SOFC hybrid system is carried out with a simulation tool that includes internal built-in functions, system components, and a thermodynamic database. The Peng-Robinson equation of state is employed for simulating processes involving solid species in equilibrium with the vapour-liquid system. The simulation is performed at a steady state.

The solar CLMR-SOFC system is modelled with the following main assumption:

- The environmental conditions are imposed at 25 °C and 1 bar.
- All components are adiabatic, with uniform pressure and temperature distribution, no equipment pressure losses and stable operating conditions of all components.
- Compressors and pumps have an isentropic efficiency of 0.82, while the mechanical efficiency is assumed to be 0.95 [22]
- Solar energy is stored for 8 h per day while the rest of the system operates 24 h per day.
- The proposed configuration is simulated with 1 kmol/hr of CH_4.

3.1. Modelling approach of solar chemical looping methane reforming thermochemical cycle

The energy storage side of the plant mainly consists of the reduction reactor of the solar CLMR and the CSP. Ceria has been widely reported as a potential candidate to activate the thermochemical redox loop due to good kinetics, fast ionic diffusivity and high cyclic efficiency, high oxygen storage capacity [25], mechanical resistance and retention of its chemical and structural properties even at high temperature [26]. As a result, it has been chosen as the OC material for the chemical looping system.

Solar energy storage takes place inside the reduction reactor, which is heated by solar radiation. The endothermic reduction of the CeO_2 and methane reforming take place according to the following reaction:

$$CeO_2 + \delta CH_4 \xrightarrow{Non-stoichiometric\ reduction} CeO_{2-\delta} + \delta(2H_2 + CO) \quad (1)$$

Several authors have carried out many experiments on the chemical reduction and oxidation of ceria. Welte et al. carried out an experimental campaign employing a 2-kW thermal solar reactor for ceria reduction using methane. They observed methane reformed with $\frac{H_2}{CO} = 2$ (partial oxidation), while the non-stoichiometric δ was 0.25 at 1300 °C [27]. Warren et al. performed experiments with a thermogravimetric analyser between 750 and 1050 °C. Starting from 900 °C they have observed the simultaneous methane reforming and ceria reduction achieving the non-stochiometric coefficient δ of 0.5 [4].

In the present analysis, a stoichiometric reduction reaction has been assumed, as shown in Eq. (2), and a study of how the non-stoichiometric coefficient affects the efficiency of the system has been implemented.

$$2CeO_2 + CH_4 \xrightarrow{Stoichiometric\ reduction} Ce_2O_3 + 2H_2 + CO \quad (2)$$

Reduced ceria and produced syngas are stored in their respective storage tanks. When energy is required, some of the reduced materials and the off-gas are sent to the oxidation reactor. The exothermic oxidation of the reduced ceria is assumed to be complete, and the water and carbon dioxide splitting reactions are assumed to occur:

$$Water\ splitting\ Ce_2O_3 + H_2O \rightarrow 2CeO_2 + H_2 \quad (3)$$

$$CO_2\ splitting\ Ce_2O_3 + CO_2 \rightarrow 2CeO_2 + CO \quad (4)$$

In this way, both steps of the chemical looping produce syngas from the reduction reactor and hydrogen and/or carbon monoxide from the oxidation reactor. A sensitivity analysis was carried out to investigate the effect of the operating parameters on the key performance indicators (KPIs) of the system. The operating parameters that were modified include (i) the fuel reforming ratio (FRR) which is the molar flow ratio between methane and ceria oxide into the reduction reactor ($\dot{n}_{CH_4}/\dot{n}_{CeO_2}$); and (ii) the co-splitting ratio (CSR) between water and carbon dioxide into the oxidation reactor ($\dot{n}_{H_2O}/\dot{n}_{CO_2}$), and (iii) the non-stoichiometric coefficient (δ) which was varied between 0.15 and 0.5 according to different literature results. The operating conditions of the CL system and a range of the parameters changed in the sensitivity analysis are summarized in Table 1.

The KPIs of the solar CLMR system are the chemical looping efficiency, the solar-to-fuel energy conversion efficiency and the energy upgrade factor. Sensible heat demand and supply are not included in these parameters. However, they are incorporated into the pinch analysis described in the following sections.

The chemical looping efficiency depicts the thermodynamic performance of the two reactors. It is defined as the ratio of the total chemical energy content at the outlet of the two reactors to the total energy input (i.e., solar energy + chemical energy of methane) and it is calculated as Eq. (5).

Table 1
Operating conditions of chemical looping sub-system.

Parameters	Values
Reactors temperature [°C] [4]	900
Reactors pressure [bar][4]	1
FRR[−]	0.1–5
δ [-]	0.15–0.5
$\dot{n}_{CH4}$ in reduction reactor [kmol/h]	1
Streams inlet temperature in main reactors [°C]	650
CSR[-]	0-∞
Operating time of reduction reactor (t_r) [h]	8
Operating time of oxidation reactor (t_o) [h]	24
Base case	
FRR[-]	0.5
δ [-]	0.5
CSR[-]	∞

Table 2
Optical end thermal efficiencies of the concentrated solar power.

Parameters	Symble	Values
Heliostat reflectivity [30]	η_{ref}	93 %
Heliostat clean factor [30]	η_{clc}	95 %
Heliostat field efficiency [30]	η_{fld}	76 %
Interception factor [30]	η_{int}	99 %
Optical efficiency	η_{opt}	66.5 %
Receiver thermal efficiency [29]	η_{rec}	80.5 %
CSP efficiency	η_{CSP}	53.5%

$$\eta_{CL} = \frac{\left(\left(\dot{n}_{H_2,red}{}^{*}t_{red} + \dot{n}_{H_2,oxy}{}^{*}t_{oxy}\right){}^{*}LHV_{H_2}\right) + \left(\left(\dot{n}_{CO,red}{}^{*}t_{red} + \dot{n}_{CO,oxy}{}^{*}t_{oxy}\right){}^{*}LHV_{CO}\right) + \left(\dot{n}_{CH_4,out}{}^{*}t_{red}{}^{*}LHV_{CH_4}\right)}{\left(Q_{sol} + \dot{n}_{CH_4,in}{}^{*}t_{red}{}^{*}LHV_{CH_4}\right)} \quad (5)$$

$\dot{n}_{H_2,red}$, $\dot{n}_{H_2,oxy}$, $\dot{n}_{CO,red}$ and $\dot{n}_{CO,oxy}$ are the molar fluxes of hydrogen and carbon dioxide produced into the reduction and oxidation reactors, respectively, $\dot{n}_{CH_{4,out}}$ is the mole flow rate of unreacted methane contents from the reduction reactor while $\dot{n}_{CH_{4,in}}$ is the inlet methane mole flow rate and Q_{sol} is the incident solar radiation on the plane of the heliostat. LHV is the lower heating value expressed in [kWh/kmol] and t_{red} and t_{oxy} are the operating times of reduction and oxidation reactors, respectively.

The solar-to-fuel energy conversion is very similar to the previous one, but it doesn't take into account the chemical energy of the unreacted methane among the outputs, while among the inputs, in addition to the solar energy, only the chemical energy of the converted methane fraction is considered, as defined in the literature [28].

$$\eta_{StF} = \frac{\left(\left(\dot{n}_{H_2,red}{}^{*}t_{red} + \dot{n}_{H_2,oxy}{}^{*}t_{oxy}\right){}^{*}LHV_{H_2}\right) + \left(\left(\dot{n}_{CO,red}{}^{*}t_{red} + \dot{n}_{CO,oxy}{}^{*}t_{oxy}\right){}^{*}LHV_{CO}\right)}{\left(Q_{sol} + \left(\dot{n}_{CH_4,in} - \dot{n}_{CH_4,out}\right){}^{*}t_{red}{}^{*}LHV_{CH_4}\right)} \quad (6)$$

Finally, the energy upgrade factor expresses the increase in the chemical energy produced in the two reactors thanks to solar energy, compared to the chemical energy contained in the initial methane.

$$U = \frac{\left(\left(\dot{n}_{H_2,red}{}^{*}t_{red} + \dot{n}_{H_2,oxy}{}^{*}t_{oxy}\right){}^{*}LHV_{H_2}\right) + \left(\left(\dot{n}_{CO,red}{}^{*}t_{red} + \dot{n}_{CO,oxy}{}^{*}t_{oxy}\right){}^{*}LHV_{CO}\right) + \left(\dot{n}_{CH_4,out}{}^{*}t_{red}{}^{*}LHV_{CH_4}\right)}{\dot{n}_{CH_4,in}{}^{*}t_{red}{}^{*}LHV_{CH_4}} \quad (7)$$

3.2. Concentrated solar power

The concentrated solar power system consists of several sun-tracking mirrors (i.e., the heliostat field) to concentrate the solar radiation onto the reduction reactor which acts as an external solar tower-mounter receiver. The heliostat field provides the heat required to reform the methane and reduce the cerium oxide. The received solar radiation (Q_{sol}) can be obtained by Eq. (8):

$$Q_{sol} = DNI{}^{*}A_{mirror} \quad (8)$$

Part of the direct normal irradiance (DNI) hitting the surface of the heliostat field (A_{mirror}) cannot reach the receiver due to optical losses (η_{opt}). Therefore, the radiative energy entering the receiver aperture (Q_{rec}) is defined by Eq. (9). The optical losses take into account the heliostat reflectivity (η_{ref}), the heliostat clean factor (η_{clc}), the heliostat field efficiency (η_{fld}) and the interception factor (η_{int}).

$$Q_{rec} = Q_{sol}{}^{*}\eta_{opt} \quad (9)$$

The CSP efficiency also take into account the thermal efficiency of the receiver (η_{rec}). An analysis of the solar receiver performance for chemical looping operating at 900 °C for the oxygen carrier reduction was assessed by Zhiwen Ma et al and values between 0.8 and 0.85 were obtained [29]. In this analysis, an assumed value of 80.5 % was utilized. The main assumptions for the heliostat field and the solar tower reduction reactor are listed in Table 2. Therefore, the solar energy required to drive the reduction reaction of the ceria oxide and reform the methane is obtained as follows:

$$Q_{red} = DNI{}^{*}A_{mirror}{}^{*}\eta_{CSP} \quad (10)$$

$$\eta_{CSP} = \eta_{opt}{}^{*}\eta_{rec} \quad (11)$$

$$\eta_{opt} = \eta_{ref}{}^{*}\eta_{clc}{}^{*}\eta_{fld}{}^{*}\eta_{int} \quad (12)$$

The minimum required storage volume (i.e., the sum of the CeO_2

Table 3
GA parameters.

Population size	200
Number of generations	200
Number of genes in each population member	4
Crossover probability	0.8
Mutation probability	0.8
Number of trials	5

volume, Ce_2O_3/CeO_2 volume and syngas volume), was estimated using a Genetic Algorithm (GA) developed in the MATLAB simulation environment. The inputs to the GA were the solar reduction energy consumption ($kJ/kmol_{Ce_2O_3}$) which varies with different values of FRR and δ, and hourly DNI data. The variables that minimise the objective function (V_{stor}) are the heliostat surface area, and the initial volumes ($V_{stor}(t_0)_j$) of CeO_2, Ce_2O_3/CeO_2 and syngas, assuming that the oxidation reactor and SOFC operate continuously without shutdowns. A more detailed description of the optimisation algorithm can be found in the Supporting Material while the GA parameters used in this analysis are listed in Table 3.

The storage tanks volumes were dimensioned according to the equations below:

$$V_{stor}(t)_j = \int_{t0}^{t} (\dot{V}_{in,j} - \dot{V}_{out,j})dt + V_{stor}(t_0)_j \quad (13)$$

$$V_{stor,j} = max(V_{stor}(t)_j) \quad (14)$$

$$V_{stor} = \sum V_{stor,j} \quad (15)$$

where $\dot{V}_{in/out,j}$ is the inlet/outlet volume flow rate of the j-reactants (i.e., CeO_2, Ce_2O_3/CeO_2, and syngas), t_0 is the assumed initial timestep and $V_{stor,j}$ is the volume size of each component. The assumed plant location is Partanna (Trapani), in Italy, where a linear Fresnel solar power plant with a nominal capacity greater than 4 MW is under construction [31]. The representative hourly DNI data were obtained from the open access tool PVGIS [32], taking into account the typical meteorological year data of the selected site (see Fig. 3).

3.3. Modelling approach of solid oxide fuel cell

The plant incorporates a SOFC module capable of directly converting the reaction enthalpy of fuel and air into electrical energy through electrochemical reactions. The air enters the SOFC from the cathode side and is reduced to oxygen ions (Eq. (16), which are then transported through the electrolyte to the anode side. Here the reaction with the hydrogen takes place (Eq. (17)) and the electrons useful for the production of electrical energy and the subsequent ionization of the oxygen are produced.

Table 4
Electrochemical model of the SOFC.

Ohmic losses	
$R_{cell,Ohm} = R_{ICA} + R_{ICC} + f_c * R_{ELY}$	21
$R_{ELY} = \frac{h_{ely}}{\sigma_{0,Ely} * exp^{-\frac{E_{A,Ely}}{RT}}}$	22
Activation losses	
$j = j_{0,an}\left[exp^{\frac{2F}{RT} * \eta_{act,an}} - exp^{-\frac{F}{RT} * \eta_{act,an}}\right]$	23
$j = j_{0,cat}\left[exp^{\frac{F}{2RT} * \eta_{act,cat}} - exp^{-\frac{F}{2RT} * \eta_{act,cat}}\right]$	24
$j_{0,an} = \frac{RT}{3F} * \sigma_{0,an} * exp^{-\frac{E_{A,an}}{RT}}$	25
$j_{0,cat} = \frac{2RT}{F} * \sigma_{0,cat} * exp^{-\frac{E_{A,cat}}{RT}}$	26
Diffusion losses	
$D_{H_2-H_2O} = \frac{1.43*10^{-7} * T_{an}^{1.75}}{p_{an}\sqrt{\frac{2}{M_{H_2}^{-1} + M_{H_2O}^{-1}} * \left(V_{d,H_2}^{\frac{1}{3}} + V_{d,H_2O}^{\frac{1}{3}}\right)^2}}$	27
$D_{m,i} = \frac{1 - x_i}{\frac{x_i}{D_{a-b}}}$ *with* $i = H_2, H_2O.$	28
$D_{Kn,i} = \frac{d_p}{3}\sqrt{\frac{8RT}{\pi * M_i}}$ *with* $i = H_2, H_2O.$	29
$D_{eff,i} = \frac{\varepsilon}{\tau}\frac{D_{m,i} * D_{Kn,i}}{D_{m,i} + D_{Kn,i}}$ *with* $i = H_2, H_2O.$	30
$p_{H_2,ely} = x_{H_2,eq} * p_{an} - \frac{R * T_{an} * j * h_{an}}{2F * D_{eff,H_2}}$	31
$p_{H_2O,ely} = x_{H_2O,eq} * p_{an} + \frac{R * T_{an} * j * h_{an}}{2F * D_{eff,H_2O}}$	32
$\eta_{Diff,an} = \frac{RT}{2F} * ln\left(\frac{x_{H_2,eq} * p_{H_2O,ely}}{x_{H_2O,eq} * p_{H_2,ely}}\right)$	33

$$\frac{1}{2}O_2 + 2e^- \rightarrow O^{2-} \quad (16)$$

$$H_2 + O^{2-} \rightarrow H_2O + 2e^- \quad (17)$$

Alternative fuels, such as CH_4, H_2O, CO, and CO_2, can be converted into SOFC through indirect conversion methods facilitated by the high temperature within the system and the inclusion of nickel in the anode

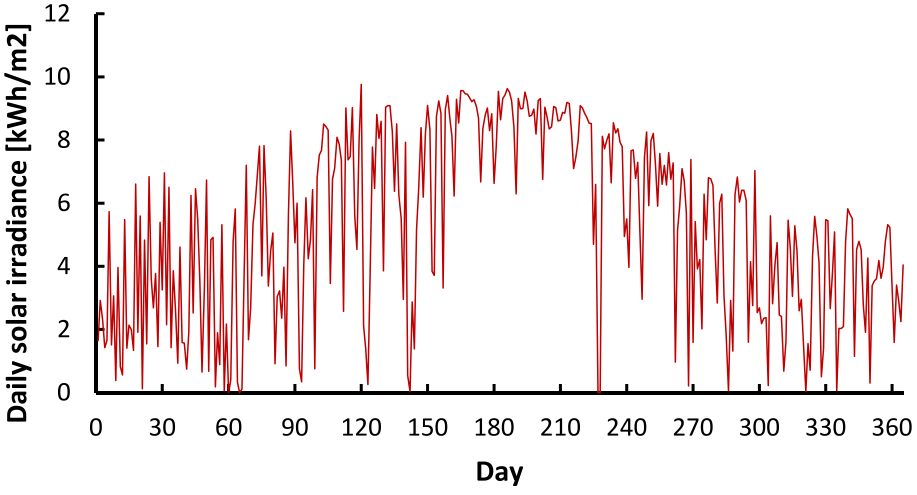

Fig. 3. Daily solar irradiance [kWh/m^2] for a typical meteorological year at Partanna, Trapani, Italy.

side. Nickel serves as a catalyst in this process. As a result, steam methane reforming (SMR), dry methane reforming (DMR), and water gas shift (WGS) reactions can occur when these substances react together.

$$\text{SMR } CH_4 + H_2O \rightarrow 3H_2 + CO \quad (18)$$

$$\text{DMR } CH_4 + CO_2 \rightarrow 2H_2 + 2CO \quad (19)$$

$$\text{WGS } CO + H_2O \rightarrow H_2 + CO_2 \quad (20)$$

The evaluation of electrochemical reactions in SOFC operations involves modelling complex phenomena. The following aspects have been assessed: (i) ohmic losses, caused by the resistance of electronics and ions migration; (ii) activation losses which occur during electrochemical reactions at the electrodes; and (iii) diffusion losses connected to the limitations of mass transport reactants.

Assumptions made in the model include:

- The cathodic compartment receives air comprising 21 % oxygen and 79 % nitrogen (N_2).
- Neglecting pressure drops across the component.
- Internal reforming of the fuel reaching chemical equilibrium.
- Only H_2 is electrochemically oxidized, and all CO is assumed to be converted via the water gas shift (WGS) reaction into H_2 [21].
- A constant voltage operating strategy is employed [17].
- Neglecting voltage drops caused by mass transport limitation on the cathode [33] with only H_2 and H_2O diffuse through the porous anode.

The correlations used to calculate the voltage drops in the cell due to the polarization losses are presented in Table 4. The electrochemical model employed follows the model described by Tjaden et al. [17].

The activation voltages on both sides of the cell are determined using the Butler-Volmer equation (Eqs. (23) and (24)). To calculate the activation voltage on the cathode side ($\eta_{act,cat}$) the hyperbolic sine expression is applied and Eq. (24) is rearranged accordingly. However, to solve the implicit Eq. (23), a simplified expression was utilized [34]:

$$\eta_{act,an} = \frac{RT}{2F} * sinh^{-1}\left(\frac{j}{2j_{0,an}}\right) \quad (34)$$

Table 5
Parameters used in the electrochemical model.

Contact loss interconnect anode $R_{ICA}[\Omega cm^2]$ [33]	0.03
Contact loss interconnect cathode $R_{ICC}[\Omega cm^2]$ [33]	0.10
Current collection correction factor f_{CC} [33]	4
Electrolyte thickness $h_{ely}[cm]$ [35]	0.001
Pre exponential factor $\sigma_{0,Ely}\left[\frac{S}{cm}\right]$ [33]	372.33
Activation energy $E_{A,Ely}\left[\frac{J}{mol}\right]$ [33]	79,535
Activation energy $E_{A,an}\left[\frac{J}{mol}\right]$ [35]	106,000
Activation energy $E_{A,cat}\left[\frac{J}{mol}\right]$ [35]	101,205
Pre exponential factor $\sigma_{0,an}\left[\frac{S}{cm}\right]$ [33]	433,033
Pre exponential factor $\sigma_{0,cat}\left[\frac{S}{cm}\right]$ [33]	61,527,821
Pressure anode side $p_{an}[Pa]$	110,000
Molar mass of hydrogen $M_{H_2}\left[\frac{g}{mol}\right]$	2
Molar mass of water $M_{H_2O}\left[\frac{g}{mol}\right]$	18
V_{d,H_2} [36]	7.07
V_{d,H_2O} [36]	12.7
Pore diameter $d_p[cm]$ [35]	0.000001
Porosity ε [35]	0.5
Tortuosity τ [35]	5
Anode thickness $h_{an}[\mu m]$ [35]	200

The evaluation of diffusion overvoltage considered the assumption that all CO is converted via the water gas shift (WGS) reaction into H_2. Consequently, the equivalent molar fraction of hydrogen incorporates the mole of CO, while the molar fraction of water also includes the quantity of CO_2 for simplification.

The relationship between voltage and current density can be represented by the following equations:

$$V_{op}(j) = V_{rev} - (ASRj) \quad (35)$$

$$ASR = R_{cell,Ohm} + (\eta_{act,an} + \eta_{act,cat} + \eta_{Diff,an})/j \quad (36)$$

In the given equations, the symbols represent the following parameter: V_{op} is the operating voltage of the cell [V], V_{rev} is the Gibbs voltage of the cell [V], j is the current density of the cell [A/cm^2] and ASR is the area specific resistance of the cell [Ω cm^2]. Using these equations, the current density can be determined under fixed operating voltage condition. The data utilized in the electrochemical model are summarized in Table 5.

The total current flowing into the stack is determined by the product of the fuel flow (N_{fuel}), the fuel utilization (FU), the Faradaic constant F and the number of electrons delivered during fuel oxidation: Z_{fuel}.

$$C_{total} = N_{fuel} \times FU \times F \times Z_{fuel} \quad (37)$$

The number of cells in the stack can be determined based on the specific area of the cell ($A_{cell} = 100cm^2$) and the current density of the cell. Additionally, the stoichiometric oxygen required is computed using Eq. *(39)*.

$$N_{cell} = \frac{C_{total}}{j^* A_{cell}} \quad (38)$$

$$\dot{n_{O_2}} = \frac{C_{total}}{4 \times F} \quad (39)$$

In high-temperature SOFC, the FU can vary between 70 % and 85 %. There is an important limitation regarding the methane concentration in the gas inlet. The maximum amount of CH_4 is typically kept below 40–50 % of the overall electrochemical reactive fuel. This limit is imposed to prevent solid carbon formation on the Ni-anode-supported stacks and guarantees a tolerable thermal gradient within the cell [17].

To establish an efficient modelling environment, all the calculations are linked with the simulation model. A sensitivity analysis was conducted, and the design parameters are represented in Table 6. The minimum fuel inlet temperature was chosen based on the recommendation provided by the ternary graph which takes into account the fuel

Table 6
Design parameters for the process model of the SOFC.

Parameters	Values
Environmental temperature [°C]	25
Environmental pressure [bar]	1.013
SOFC temperature [°C]	600–900
SOFC pressure [bar]	1.1
Cell voltage [V]	0.6–0.9
Faraday's constant [C/mol]	96,485
DC/AC inverter efficiency	0.95
Steam-to-carbon ratio, S/C [4,25]	1–4
Fuel utilisation	0.7–0.85
Air c_p, kJ/kg. k	1.005
Air molecular weight (g/mol)	27.2
Compressor isentropic efficiency	0.9
Compressor mechanical efficiency	0.85
Fuel compressor efficiency	0.90
Base case	
SOFC temperature [°C]	800
Cell voltage [V]	0.8
Fuel utilisation	0.85
Steam-to-carbon ratio, S/C	2

composition, to avoid carbon deposition.

In the anode of the SOFC, the reactions taking place are exothermic. To maintain thermal balance within the stack, air is supplied. A portion of the heat generated by these exothermic reactions is utilized for internal reforming reactions, while the remaining heat is dissipated through the air. To determine the amount of air required in the cathode compartment, calculations are performed by applying a thermal balance analysis on the SOFC system. This balance takes into account all the heat sources and heat sinks resulting from the electrochemical reactions occurring within the stack. By considering these factors, the appropriate amount of air can be determined to achieve thermal equilibrium in the SOFC system.

$$Q_{Produced} = \Delta H_{reaction} - W_{electrical} \quad (40)$$

$$Q_{Produced} = Q_{Air} + Q_{Reformer} \quad (41)$$

$$Q_{Air} = Q_{Produced} - Q_{Reformer} \quad (42)$$

$$Q_{Waste} = Q_{Air} = \Delta H_{reaction} - W_{electrical} - Q_{Reformer} \quad (43)$$

$$W_{electrical} = V.\ C_{total} \quad (44)$$

Eq. (40) is delivered from the first law of thermodynamics. It describes the change in enthalpy (Δ H) within the anode. This change in enthalpy is separated into two distinct components: one part of it is utilised to generate electricity, while the remainder is transformed into thermal energy. The heat generated within the system is regulated through a dual process: dissipation of heat through air and the heat demand of the reformer, as shown in Eq. (41). To evaluate the amount of heat removed by air (denoted as waste heat, Q_{waste}) the total enthalpy changes across the anode, the electric power generated, and the heat demanded by the reformer were considered. This relationship is expressed in Eq. (43). It is important to note that the primary purpose of supplying air is to remove the excess heat left after the endothermic reforming reaction. The electrical power generated in the SOFC system can be calculated using Eq. (44).

3.4. Modelling approach of oxy-fuel combustion

The afterburner is modelled as an adiabatic reactor, converting the chemical energy of the SOFC exhaust to thermal energy. The specific operating conditions for the oxyfuel combustion section can be found in Table 7. The SOFC off-gas (i.e., CH_4, H_2, CO, H_2O, and CO_2) reacts with pure oxygen converting the unreacted fuel in H_2O and CO_2. To achieve an outlet temperature of 900 °C for the afterburner, a heat exchanger is incorporated. This heat exchanger allows the heat generated in the oxy-combustion unit to be transferred to the air that is fed to the cathode side of the SOFC, contributing to temperature control and overall system efficiency.

Oxy-fuel process is recognized as an efficient method for capturing CO_2. However, it is important to note that this technology is associated with an energy-intensive process known as air separation. A commercial ASU unit typically requires an energy consumption of (W_{ASU}) 0.25 kWh/kg O_2 [37]. To simplify the system, a stoichiometric approach is considered. Additionally, the assumption is made that pure oxygen is generated through the ASU and only methane (i.e., no natural gas) fed the system. While this assumption is not realistic, it's important to note that in practice, oxygen purity typically falls within the range of 99.5 % to 95 %. The energy consumption for oxygen production in this context typically varies from 0.35 to 0.2 kWh/kgO_2 [38]. This simplification approach has been adopted by various researchers [39].

Table 7
Operating condition of the oxyfuel combustion unit.

Operating parameter	values
Oxy-fuel afterburner	
Combustion pressure, [bar]	1
Inlet oxygen temperature, [°C]	25
Inlet anode off-gas temperature, [°C]	800
Afterburner outlet temperature, [°C]	900

Table 8
Operating parameter of syngas and CO2 storage compression unit.

Operating parameter	values
Syngas Storage	
Syngas storage pressure, [bar]	60
Compressor isentropic efficiency	0.82
Compressor mechanical efficiency	0.94
Compression ratio per inter-cooled stage	2.8
Cooler outlet temperature, °C	25
CO_2 compression and storage	
Compressed CO_2 pressure, [bar]	150
Compression ratio per inter-cooled stage	2.72
Compressor isentropic efficiency	0.82
Compressor mechanical efficiency	0.94
Cooler outlet temperature, °C	25

3.5. Modelling approach of syngas and carbon storage compression unit

Throughout daylight hours, when sunlight is abundant, the proposed plant undergoes substantial syngas production. Nevertheless, in order to counteract the intermittent nature of solar energy, a syngas storage unit has been integrated into the plant's design. Furthermore, it is essential for the stable operation of the SOFC. The SOFC is sensitive to load disruptions and fuel interruptions, and a storage unit helps mitigate these issues. To achieve this, a compressor train is utilized with a constant compression ratio. Additionally, an intercooler is implemented to recover the heat from the syngas and enhance compression efficiency. Following the oxyfuel combustion section, the CO_2 generated is directed to the compression unit. There, it undergoes pressurization to 150 bar before being transferred to permanent storage. Table 8 outlines the key operational parameters of the storage system.

3.6. Design of heat exchanger network with pinch analysis

Pinch analysis is a widely used methodology for evaluating the minimum external thermal energy requirement of different plant configurations. In the context of the proposed plant systems, pinch analysis is conducted independently for energy storage and release units. This separation arises due to the temporal availability of solar thermal energy, and thus, performing separate pinch analyses for these sections is imperative to prevent the coupling of two flows operating at distinct times. This approach ensures that each component operates most effectively within the system.

During the pinch analysis, it is crucial to ensure that a minimum temperature difference of 20 °C is maintained in each coupling. This temperature difference constraint is taken into account to optimize the thermal integration within the system and ensure efficient energy utilization [40]. By conducting pinch analysis, the energy requirements and heat transfer constraints of the plant configurations can be evaluated and compared, providing insights into the overall system performance and potential improvements.

$$T_{Cold_{in}<=}T_{Hot_{out}} - 20 \quad (45)$$

$$T_{Hot_{in}>=}T_{Cold_{out}} + 20 \quad (46)$$

In addition, the surplus heat available at lower temperatures can be utilized to heat water in a district heating network (DHN) from 60 °C to 90 °C. A heat exchanger is employed for this purpose, and the minimum temperature difference considered in this heat exchanger is set at 10 °C [10]. This allows for efficient heat transfer and utilization in the DHN.

During periods when solar radiation is available, a fraction of the syngas generated in the reduction reactor is directly supplied to the

SOFC at high temperatures. However, during other times of the day, the syngas is provided by the storage system (R1 in Fig. 2) at ambient temperature. To account for these scenarios, a heat exchanger network is designed, specifically considering the worst-case scenario: (i) in the energy storage side, where syngas is directly supplied to the SOFC, the heat associated with this syngas is not available for analysis purposes; (ii) in the energy release side, where syngas is provided from the storage system, heat is required to raise the temperature of the syngas from ambient temperature to the inlet temperature of the SOFC.

By considering these aspects and analysing the heat exchanger network in both the energy storage and energy release configurations, a comprehensive assessment of the system performance and heat transfer requirements can be achieved.

3.7. Key performance indicators

Three key parameters are defined to optimize the overall system performance: electricity efficiency, electricity efficiency with carbon capture and storage (CCS), global efficiency and energy density. These parameters are calculated using the following equations:

$$\eta_{el} = \frac{W_{el}{}^{*}t_{oxy} - W_{aux}{}^{*}t_{oxy} - W_{syn}{}^{*}t_{red}}{(\dot{n}_{CH_4,in}{}^{*}LHV_{CH_4}){}^{*}t_{red} + Q_{sol}} \tag{47}$$

$$\eta_{el-CCS} = \frac{(W_{el} - W_{aux} - W_{CO_2} - W_{ASU}){}^{*}t_{oxy} - W_{syn}{}^{*}t_{red}}{\dot{n}_{CH_4,in}{}^{*}LHV_{CH_4}{}^{*}t_{red} + Q_{sol}} \tag{48}$$

$$\eta_{global} = \frac{((W_{el} - W_{aux} - W_{CO_2} - W_{ASU}){}^{*}t_{oxy} - W_{syn}{}^{*}t_{red}) + Q_{DHN,r}{}^{*}t_{red} + Q_{DHN,o}{}^{*}t_{oxy}}{\dot{n}_{CH_4,in}{}^{*}LHV_{CH_4}{}^{*}t_{red} + Q_{sol}} \tag{49}$$

$$E = \frac{\left(\left(\dot{n}_{H_2,red} + \dot{n}_{H_2,oxy}{}^{*}\frac{t_{oxy}}{t_{red}}\right){}^{*}LHV_{H_2}\right) + \left(\dot{n}_{CO,red} + \dot{n}_{CO,oxy}{}^{*}t_{oxy}/t_{red}\right){}^{*}LHV_{CO}\right) + \left(\dot{n}_{CH_{4,out}}{}^{*}LHV_{CH_4}\right)}{\dot{n}_{H_2,red}/d_{H_2} + \dot{n}_{CO,red}/d_{CO} + \dot{n}_{CH_{4,out}}/d_{CH_4} + \dot{n}_{CeO_2,red,in}/d_{CeO_2} + \dot{n}_{Ce_2O_3,red,out}/d_{Ce_2O_3}} \tag{50}$$

In above equations W_{syn}, W_{CO_2} and W_{aux} represent the power electricity required to compress syngas, CO_2 and air, respectively. While W_{el} is the electrical power output from the plant. W_{ASU} is the power required by the air separation unit. $\dot{n}_i$, LHV_i and d_i are the mole flow rate in [kmol/h], the lower heating value, and the molar density [kmol/m^3] of the component i, respectively. Q_{sol} represents the thermal energy gained from the sun while $Q_{DHN,r}$ and $Q_{DHN,o}$ are the thermal power provided to the district heating network.

These variables and parameters play crucial roles in the calculation of electricity efficiency, electricity efficiency with CCS, and global efficiency, as they represent the energy requirements, power outputs, and thermal contributions within the system. By considering these factors, the overall system performance and energy utilization can be analysed and optimized.

Table 9
Modeling results of the base case scenario.

Base case scenario	
η_{CL}	63.1%,
η_{StF}	62.6%
U	1.24
η_{el}	25.7 %
η_{el-CCS}	23.8 %
$E\left[\frac{kWh}{m^3}\right]$	215.5

4. Results and discussion

The performance of the solar chemical looping reforming energy storage system integrated with solid oxide fuel cells was analysed under various operating conditions, starting with the base case scenario. In this scenario, the mole flow rate of methane into the reduction reactor was fixed at 1 kmol/h, and the FRR parameter was initialized at 0.5. The solar methane reforming process operated for eight hours per day, generating syngas that was stored for later use. The oxidation reactor operated under the same thermodynamic conditions as the reduction reactor, with a non-stoichiometric coefficient set to 0.5. Continuous supply of water vapour to the oxidation reactor (CSR=∞) facilitated the production of excess hydrogen through stoichiometric steam interaction with reduced ceria. The initial system configuration achieved notable performance metrics, including a chemical looping efficiency of 63.1 %, solar-to-fuel efficiency of 62.6 %, and an upgrading factor of 1.24. A portion of the syngas was stored at high pressure, while the SOFC received a constant mole flow rate comprising syngas from the storage or reduction reactor and hydrogen from the oxidation reactor throughout the day. Detailed information regarding the fuel utilization, operating voltage, steam-to-carbon ratio, temperature, and pressure are provided in Table 6, offering insights into the SOFC's performance within the integrated system. These parameters serve as a reference for evaluating the SOFC's behaviour and performance under varying operating conditions and enable comparisons with other system configurations or optimization strategies. The SOFC system consistently generated 42 kW of electricity, resulting in electricity efficiency and electricity efficiency with carbon capture and storage (CCS) of 25.7 % and 23.8 %, respectively. The base case scenario results are summarised in Table 9.

The following paragraphs present the results of a comprehensive sensitivity analysis conducted on the main operating parameters of the system's components. This analysis aimed to assess the quantitative impact of individual parameters on the key performance indicators (KPIs) of the system. Through a systematic variation of these parameters and a comprehensive assessment of their impact on the KPIs, the study determined the optimal values that lead to the maximization of system efficiency.

4.1. Effect of fuel reforming ratio

The thermal reduction of ceria (CeO_2) to Ce_2O_3 is a critical process step in the system. The introduction of methane as a reducing agent enables the reduction of ceria at lower temperatures compared to conventional thermal reduction methods. The outlet stream from the reduction reactor comprises a mixture of gases (H_2, CO, H_2O, CO_2, unreacted CH_4) and solids (Ce_2O_3 and unreduced CeO_2). The primary focus is on exploring the effect of the fuel reforming ratio (FRR) parameter, which varies from 0.1 to 5 on a molar basis. The analysis considers how this parameter affects the equilibrium composition at the outlet of the reduction reactor and the KPIs of the plant.

Fig. 4 presents the equilibrium mole fraction of gaseous species (H_2, CO, CH_4, H_2O) and solid species (CeO_2, Ce_2O_3) as a function of the FRR. At lower FRR values (0.1 to 0.4), there is a higher molar fraction of H_2 and CO in the product stream, indicating a greater conversion of methane. However, a complete reduction of CeO_2 is not achieved in this range. At FRR equal to 0.5, which represents the stoichiometric

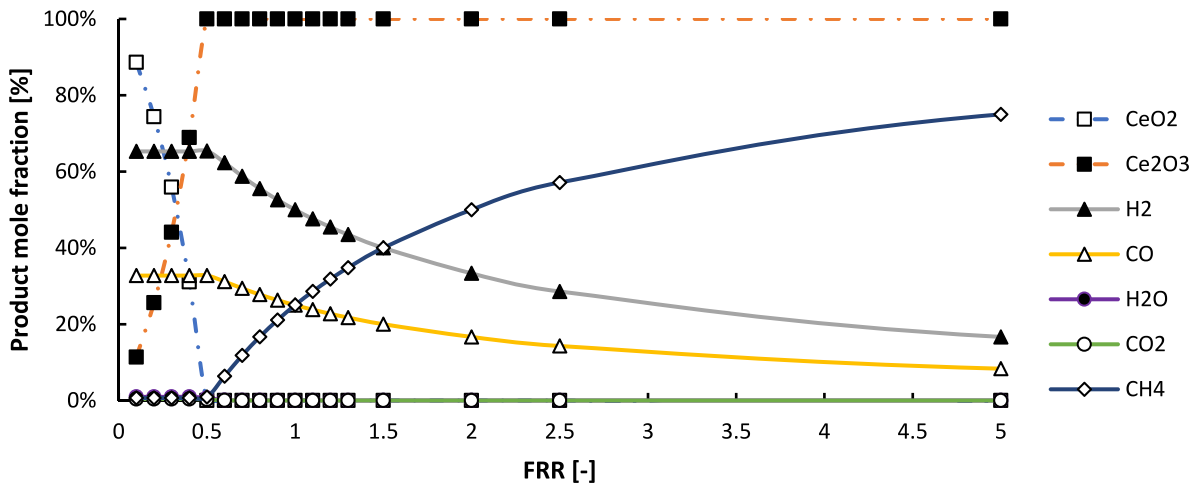

Fig. 4. The molar fraction of different species in the product stream varies with the FRR. The dotted line represents the molar fraction of completely oxidized ceria (white square) and reduced ceria (black square). The solid line represents the molar fraction of the gases produced by solar methane reforming.

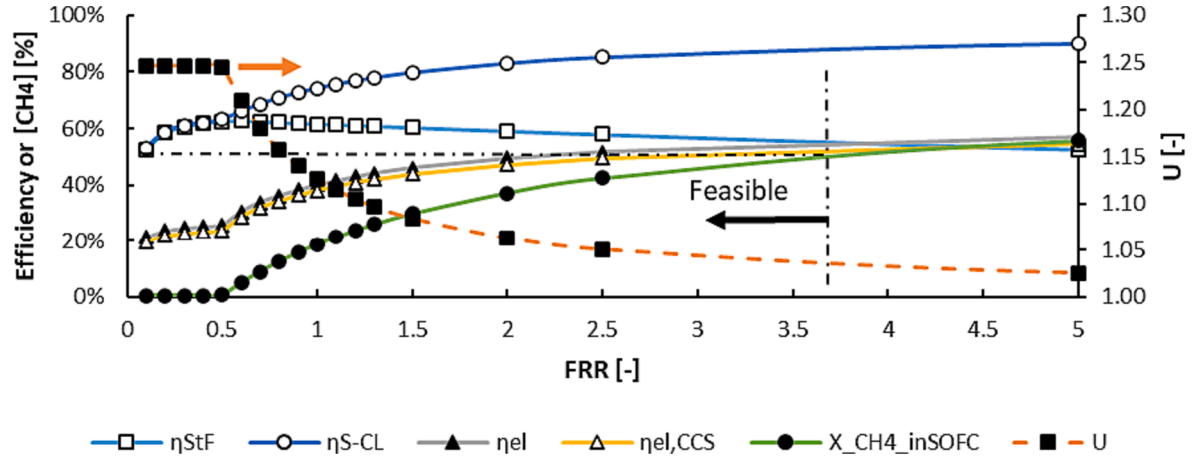

Fig. 5. On the left axis of the graph, the solar to fuel efficiency (represented by white square indicators), solar chemical looping efficiency (white circle indicators), electricity efficiency (black triangle indicators), and electricity efficiency with CCS (white triangle indicators) are plotted against the varying FRR parameter. Additionally, the methane concentration of the gas mixture fed to the SOFC is represented by white rhombus indicators. On the right axis of the graph, the values of the energy upgrade factor can be read.

reduction, the CeO_2 is fully reduced, resulting in the maximum mole fraction of H_2, and CO. Additionally, methane is completely reformed in this condition. On the other hand, increasing the FRR parameter (while keeping the molar feed ratio of methane constant) leads to a higher amount of unreacted methane and a lower quantity of reforming products. This occurs when all the oxygen carrier particles have been consumed.

Fig. 5 showcases the variations in efficiencies at different values of FRR. The efficiencies are calculated when Ce_2O_3 is oxidized using water (CSR=∞), resulting in the generation of only H_2 in the oxidation reactor. The energy upgrade factor remains relatively constant until FRR reaches 0.5. Beyond that point, U decreases due to lower methane conversion. The solar-to-fuel efficiency exhibits an increasing trend from FRR = 0.1 to FRR = 0.5, attributed to reduced sensible energy requirements for pre-heating the reactants to the reduction temperature. It peaks at FRR = 0.5 (η_{StF}= 62.6%) and then decreases due to lower conversion of methane. In contrast, the solar CL efficiency shows an upward trend because unreacted methane is considered as an output in its calculation. The electricity efficiency and electricity efficiency with CCS follow a similar trend, increasing with higher FRR values, reaching 56.8 % and 54.4 %, respectively. The difference between them remains relatively constant, ranging from 1.6 % to 2.4 %.

Fig. 5 also includes the molar CH_4 concentration of the overall electrochemical reactive fuel at the SOFC inlet. To ensure proper SOFC operation and avoid temperature gradients, this concentration should be kept below 40–50 %. An FRR lower than 2.3 is recommended for safe operation, while the maximum FRR should not exceed 4. In addition, Fig. 6 presents an equilibrium ternary diagram illustrating the inlet composition at the SOFC anode, considering the reactive fuel, H_2O, and CO_2, as a function of the FRR parameter. In the base case scenario (represented by an orange circle), the inlet temperature needs to be higher than 800 °C to prevent solid carbon deposition on the Ni-anode. However, with an FRR greater than one, a nominal inlet temperature of 750 °C is deemed safe, ensuring the absence of solid carbon formation.

It is worth noting that at the base case operating condition of the SOFC, the higher concentration of unreacted methane does not result in the deposition of carbonaceous solids. Instead, the failure of the cell can be attributed to thermal gradients alone.

An optimization algorithm was employed to minimize storage volumes and evaluate the energy density of the system for each FRR value. Fig. 7 illustrates the results of the GA on storage volume. Higher FRR values lead to a decrease in storage volume. Similarly, the surface area of the heliostat field decreases from 410 m^2 to 42 m^2. This occurs because higher FRR values result in a reduction of solar energy stored as

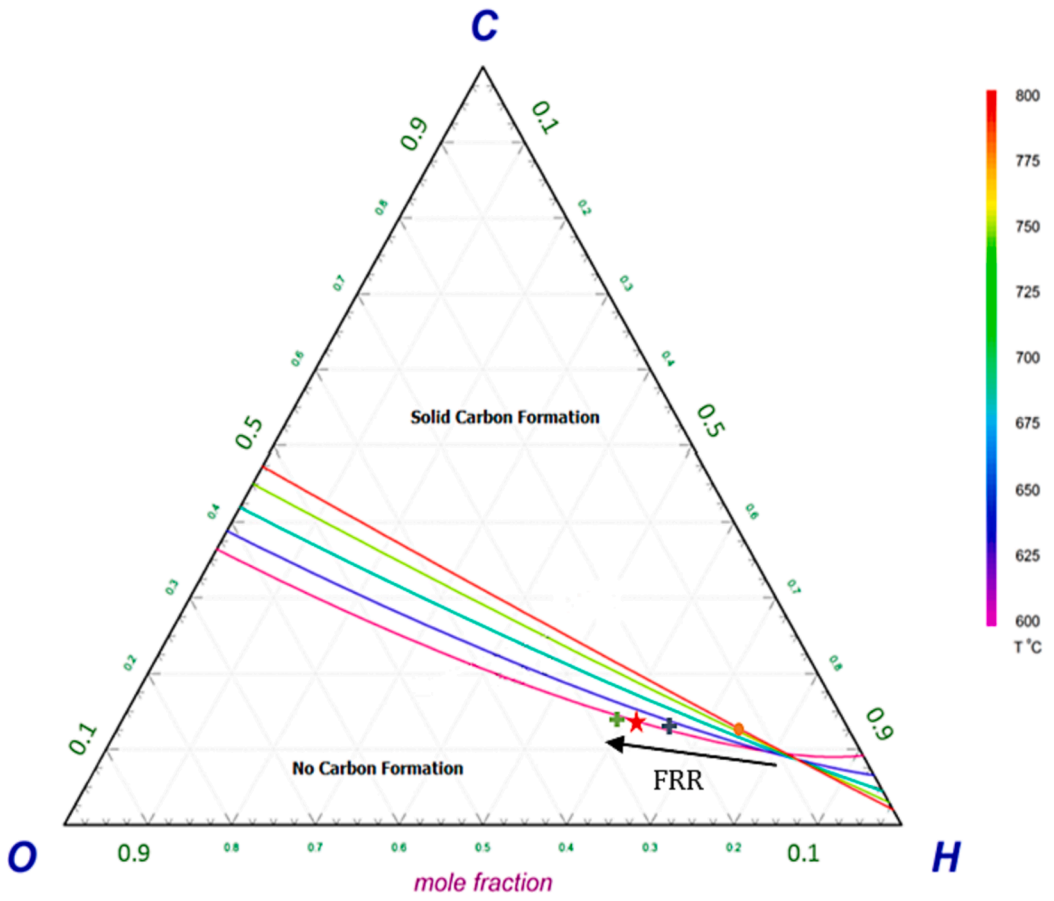

Fig. 6. Ternary C-H-O diagram for the partial oxidation reformer SOFC inlet composition. The orange circle is the base case scenario (FRR = 0.5), the blue cross is FRR = 1, the red star is FRR = 2 and the green cross is FRR = 5.

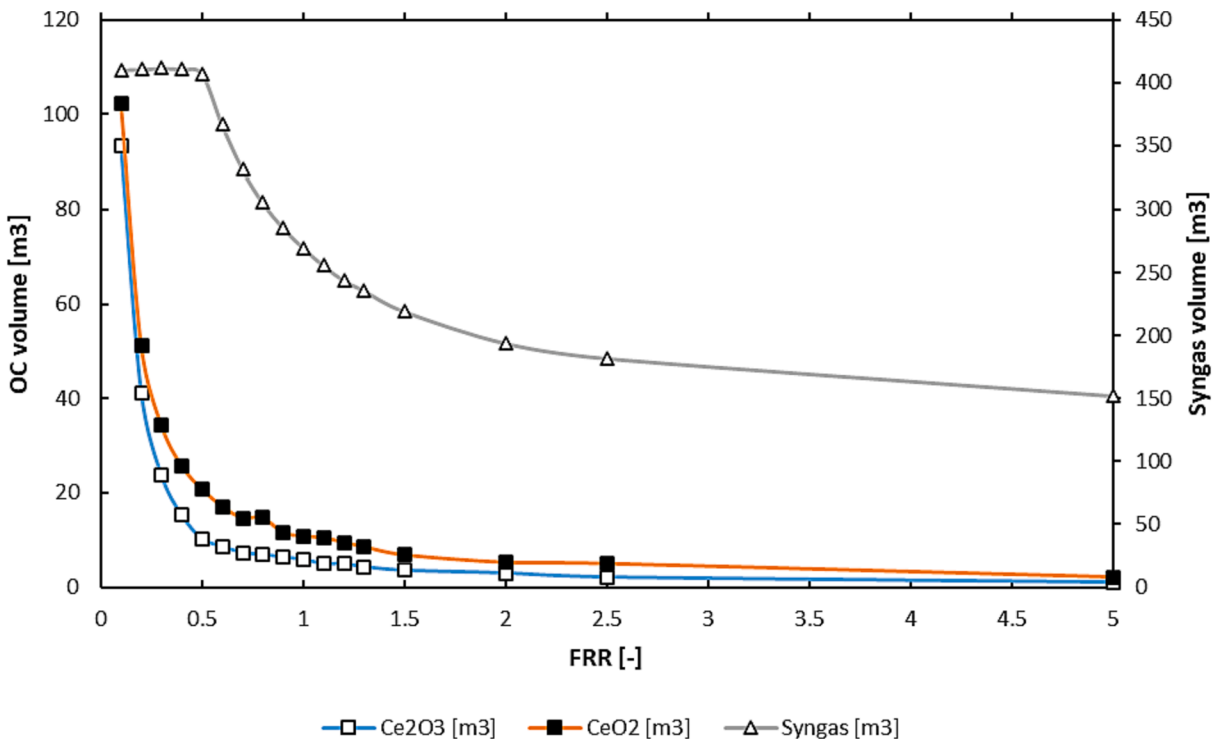

Fig. 7. The optimized storage volume achieved through the implementation of the GA.

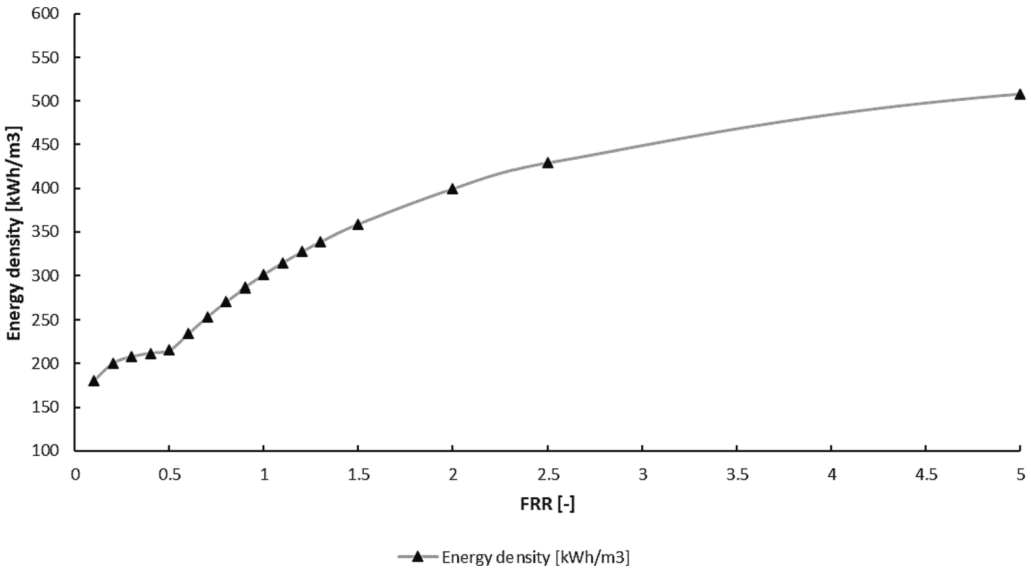

Fig. 8. Energy density of the proposed configuration system at different values of FRR.

Table 10
Effect of co-splitting ratio on KPIs.

CSR	η_{StF}	η_{S-CL}	U	η_{el}	$\eta_{el,CCS}$	$E\left[\frac{kWh}{m^3}\right]$
∞	59.1 %	83.1 %	1.06	49.4 %	47.2 %	399.4
2.25	59.5 %	83.2 %	1.07	49.6 %	47.4 %	400.2
0	61.5 %	84.1 %	1.08	49.7 %	47.5 %	404.2

chemical compounds, while the amount of unreacted methane sent to the storage increases.

The energy density is an important parameter in assessing the performance and feasibility of storage systems. Different materials and configurations can yield different energy densities, and optimization efforts are often focused on maximizing the energy density to enhance the overall efficiency and cost-effectiveness of the storage system. Fig. 8 presents the results of the sensitivity analysis conducted on the energy density. It is observed that as the FRR parameter increases, the energy density also increases. This trend can be attributed to the decrease in unreacted material at higher FRR values. In other words, by optimizing the FRR parameter, a higher energy density can be achieved, indicating a more efficient utilization of the stored energy.

The FRR parameter was adjusted from 0.5 to 2 to optimize electricity efficiency and energy density while minimizing the storage volumes. This adjustment was crucial to ensure both efficient performance and safe operation of the system.

4.2. Effect of co-splitting ratio

Three different approaches were investigated to feed the oxidation reactor stoichiometrically with H_2O, CO_2, or a combination of both. These alternatives were considered: (i) utilizing water obtained from steam condensation following complete off-gas combustion (base case with CSR=∞); (ii) employing a stream comprising a split of H_2O/CO_2 before water separation from the off-gas (CSR = 2.25); and (iii) utilizing a CO_2 stream obtained after water condensation (CSR = 0). Table 10 presents the results of the KPIs for each approach.

As the concentration of CO_2 in the oxidant stream increases and the CSR decreases, all KPIs show improvement. This is primarily due to the reuse of CO_2 within the system, resulting in reduced consumption of compression electricity. Notably, a portion of the CO_2 that was initially intended for sequestration is now utilized, leading to a beneficial effect on system performance.

The ternary diagram is used also in this case to evaluate the possible carbon formation. Fig. 9 shows how the addition of H_2, CO or a combination thereof does not greatly influence the formation of solid carbon, which is however avoided if the inlet temperature is higher than 600 °C. This led to a change in the base case from using pure water to only carbon dioxide as an oxidant.

4.3. Influence of ceria effectiveness

The physicochemical stability of OC particles is a critical factor for the successful operation of thermochemical cycles and circulated OC particles in solar reactors. Over multiple redox cycles, structural changes occur in the OC particles, and in the case of ceria, the reference material in this study, it exhibits recyclability. However, as the cycling process continues, ceria particles undergo modifications in dimensions, phase change behaviour, and particle size distribution. leading to a gradual decrease in ceria effectiveness and oxygen storage capacity [41]. To account for material degradation and variations in ceria performance, a sensitivity analysis was conducted by reducing the non-stoichiometric coefficient from 0.5 to 0.15, while maintaining FRR and CSR values at 2 and 0, respectively. Under these conditions, a portion of the ceria particles circulates without undergoing active redox reactions, resulting in altered equilibrium conditions within the reduction reactor and subsequently impacting the overall system performance.

Fig. 10 illustrates the sensitivity analysis of the chemical looping reduction reactor's output to variations in the effectiveness of the OC. At a non-stoichiometric coefficient of 0.5, the highest quantities of reformed products are obtained, with H_2, CO, and CH_4 accounting for 33 %, 17 %, and 50 % respectively. This indicates successful redox reactions facilitated by fully active cerium oxide, resulting in significant methane conversion. As the non-stoichiometric coefficient of ceria decreases, a gradual decline in reformed species production is observed, reaching its lowest point at 0.15. At this level, the storage of reduced ceria in the chemical energy storage reservoir is minimal (18 %), while a larger fraction of methane (80 %) remains unconverted. Consequently, the syngas composition exhibits lower H_2 content, and a higher proportion of methane compared to the higher non-stoichiometric coefficient.

Fig. 11 presents the results of the sensitivity analysis conducted on the KPIs of the plant and the methane concentration in the electrochemical reactants at the inlet of the SOFC. At the chosen operating

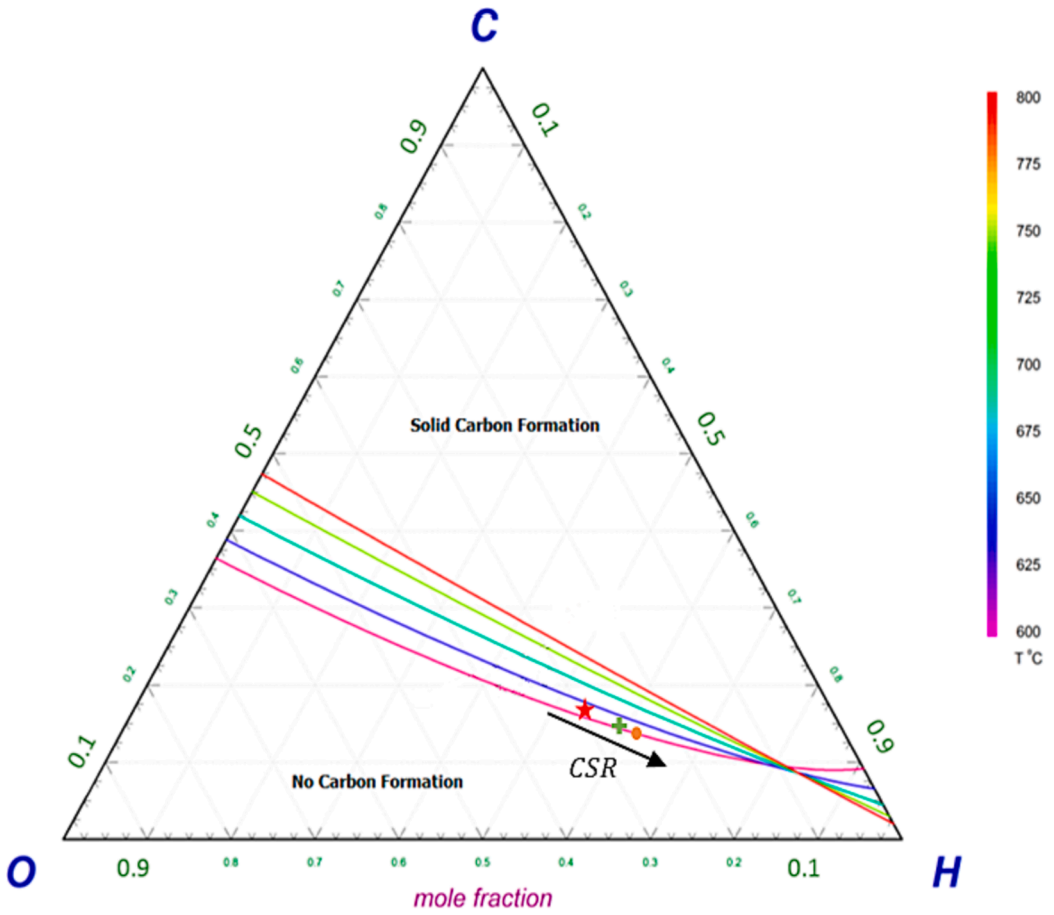

Fig. 9. Ternary C-H-O diagram for the partial oxidation reformer SOFC inlet composition varying the CSR. The orange circle is the base case scenario (CSR=∞), the green cross is CSR = 2.25 and the red star is CSR = 0.

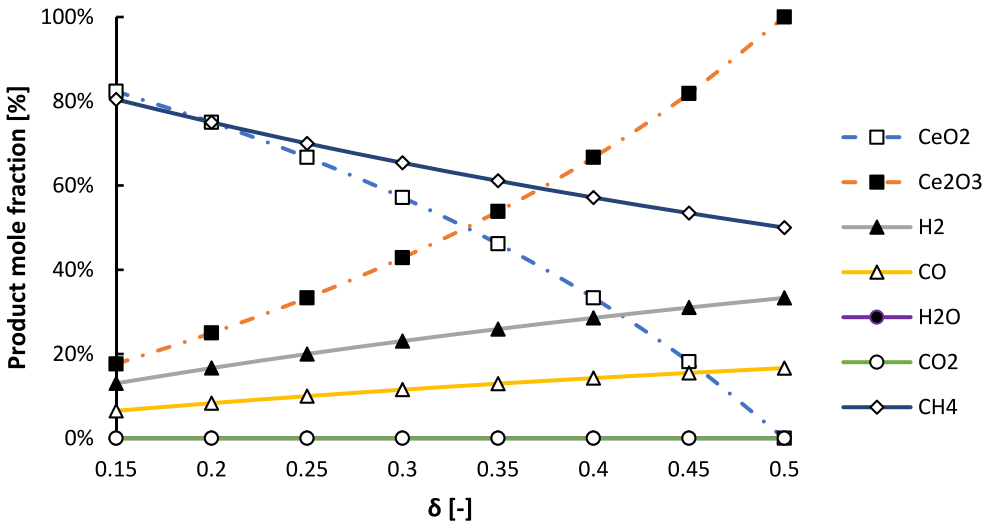

Fig. 10. Product mole fraction at different values of non-stoichiometric coefficient. The dotted line represents the molar fraction of completely oxidized ceria (white square) and reduced ceria (black square). The solid line represents the molar fraction of the gases produced by methane reforming.

conditions (FRR = 2 and CSR = 0) in the previous analysis, there is a risk of stack rupture due to a high thermal gradient caused by the elevated methane concentration when δ is less than 0.27. This indicates that if the material degrades beyond this level or if the oxygen carrier has a lower non-stoichiometric coefficient, it is necessary to increase the flow rate of ceria oxides inside the reduction reactor. Specifically, when only CO_2 is sent into the oxidation reactor with a δ of 0.15, the FRR must be adjusted to 1 to achieve a methane concentration in the reactant gas mixture fed to the SOFC that is lower than 50 % (specifically, 48 %).

At higher ceria effectiveness, redox reactions are highly activated, leading to a 25 % conversion of methane into syngas in the presence of fresh ceria. Maintaining the system in a feasible mode, a non-

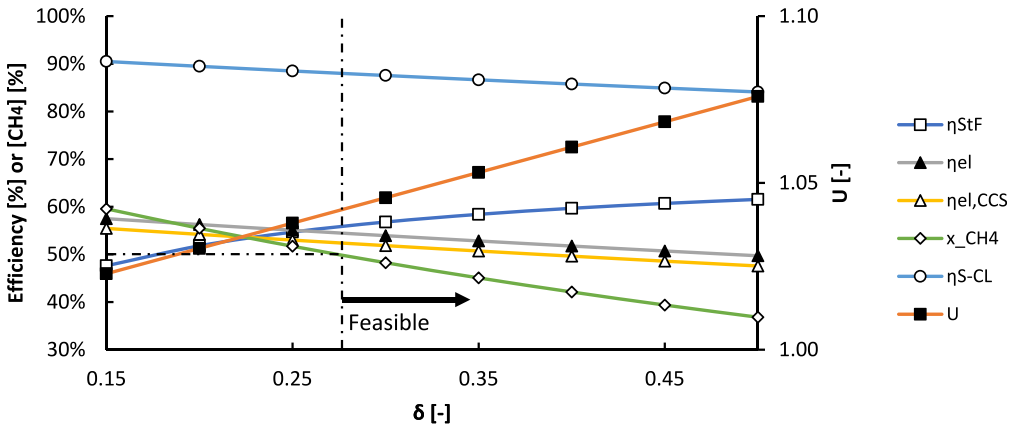

Fig. 11. The solar to fuel efficiency (white square indicator), solar chemical looping efficiency (white circle indicator), electricity efficiency (black triangle) and electricity with CCS efficiency (white triangle) and methane concentration of the reactant gas mixture fed the SOFC (white rhombus) are illustrated in the left axis varying the non-stoichiometric coefficient. Instead, the values of the energy upgrade factor (black square) can be read on the right axis.

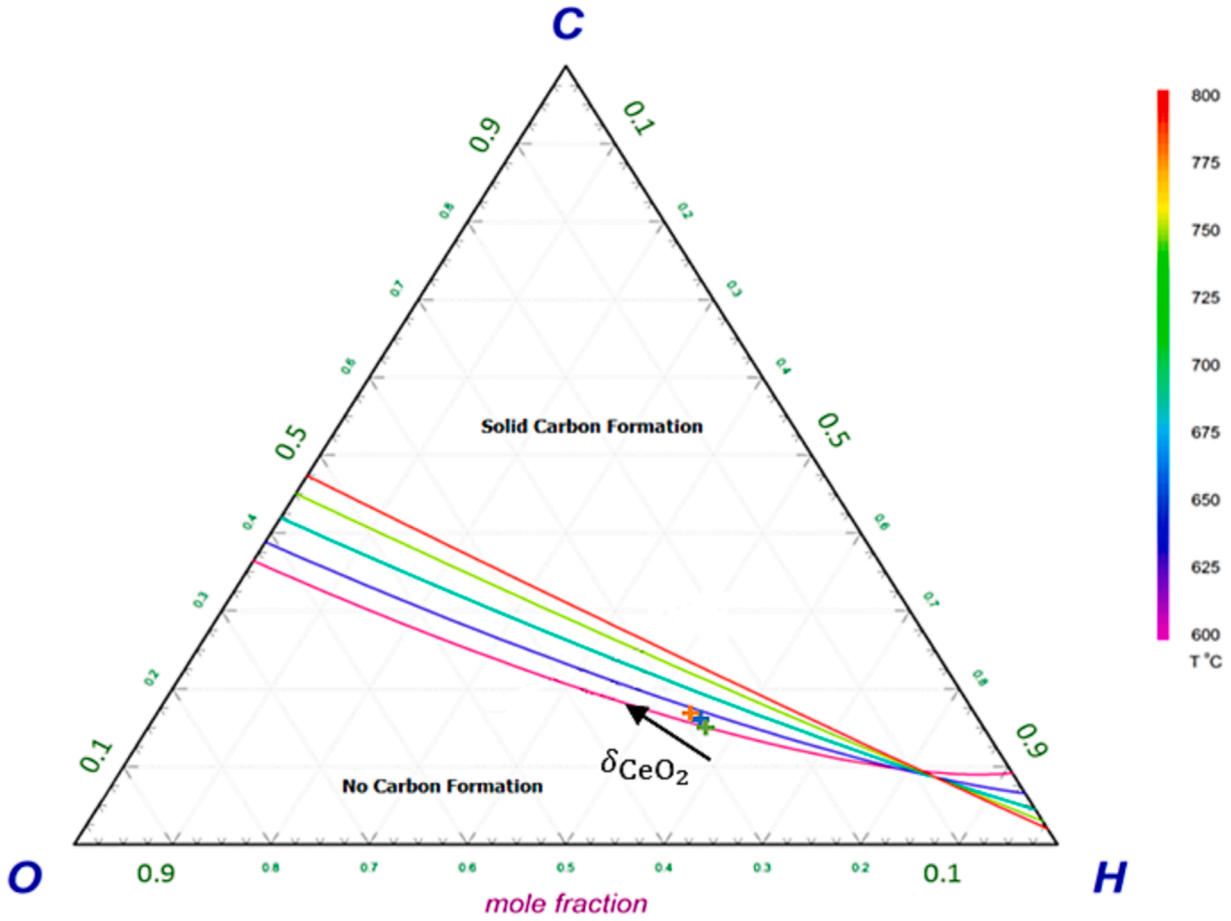

Fig. 12. Ternary C-H-O diagram for the partial oxidation reformer SOFC inlet composition varying the ceria effectiveness (non-stoichiometric coefficient). The orange cross is the nominal case in which $\delta = 0.5$, the blue cross is $\delta = 0.3$ and the green cross is $\delta = 0.15$.

stoichiometric coefficient of 0.3 results in the maximum electricity and electricity with CCS efficiencies, reaching 53.9 % and 51.8 % respectively. However, the solar-to-fuel efficiency decreased from 61.5 % to 56.8 %. A similar trend is observed for the energy upgrade factor, while the solar chemical looping efficiencies increase by 3.4 %, going from 84.1 % with $\delta = 0.5$ to 87.5 % with $\delta = 0.3$.

The analysis of FRR and δ effects on electrical efficiency indicates that the methane concentration at the inlet of the SOFC acts as the intermediary between these parameters and the key performance indicators. The results shown in Fig. 4 and Fig. 10 demonstrate that higher FRR values and lower δ values lead to lower methane conversion. Consequently, the system's efficiency increases because the recirculating gases, such as CO_2 and water vapour, facilitate the occurrence of steam methane reforming (SMR), dry methane reforming (DMR), and water–gas shift (WGS) reactions inside the SOFC, resulting in an increased molar concentration of hydrogen and higher electric power generation.

In Fig. 12 the ternary diagram demonstrates that at various δ values

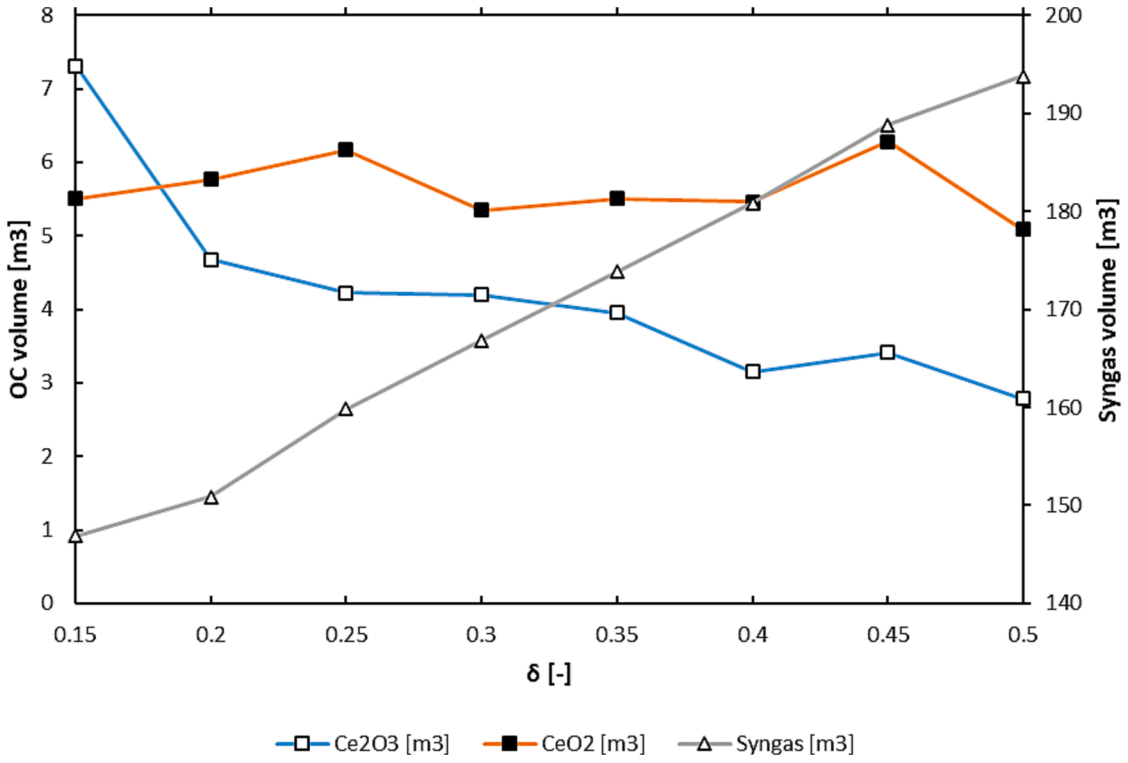

Fig. 13. The optimized storage volume achieved through the implementation of the GA at different values of δ.

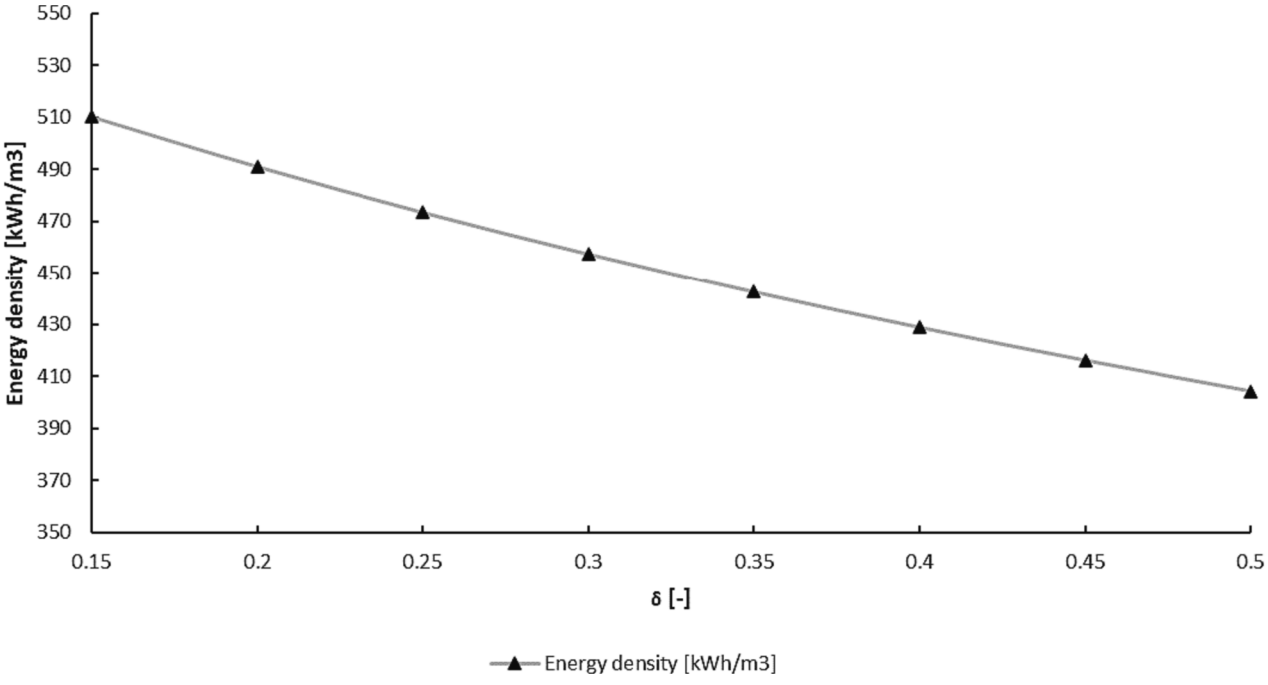

Fig. 14. Energy density of the proposed configuration system at different values of δ.

and operating temperatures above 600 °C, there is no carbon deposition observed. Consequently, the potential limitation that could lead to stack malfunction remains the methane concentration, as described earlier.

The trend of the storage volume is illustrated in Fig. 13. At different values of δ, the size of the solids storage remains relatively constant, while the volume of the syngas storage undergoes significant changes. This is because, with the higher effectiveness of the material, more methane is converted into hydrogen and carbon monoxide, leading to an increase in the storage volume of syngas.

Fig. 14 shows the relationship between the energy density of the plant and the non-stoichiometric coefficient. While the effectiveness of ceria decreases, the energy density of the system increases. This is because less methane is converted, resulting in lower solar energy storage. As a result, the energy density approaches the energy density of compressed methane.

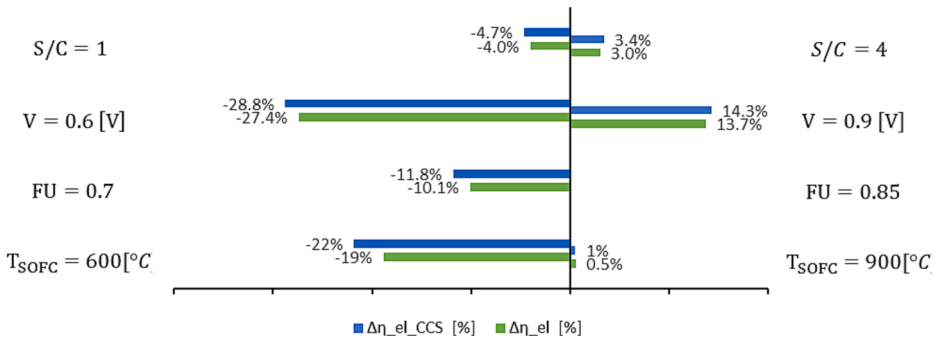

Fig. 15. Results in electrical with/without CSS efficiencies of the parametric analysis applied to SOFC operating variable. The reference values are represented by a vertical black line: (i) S/C = 2; (ii) V = 0.8 [V]; (iii) FU = 0.85; and (iv) operating temperature equal to 800 °C.

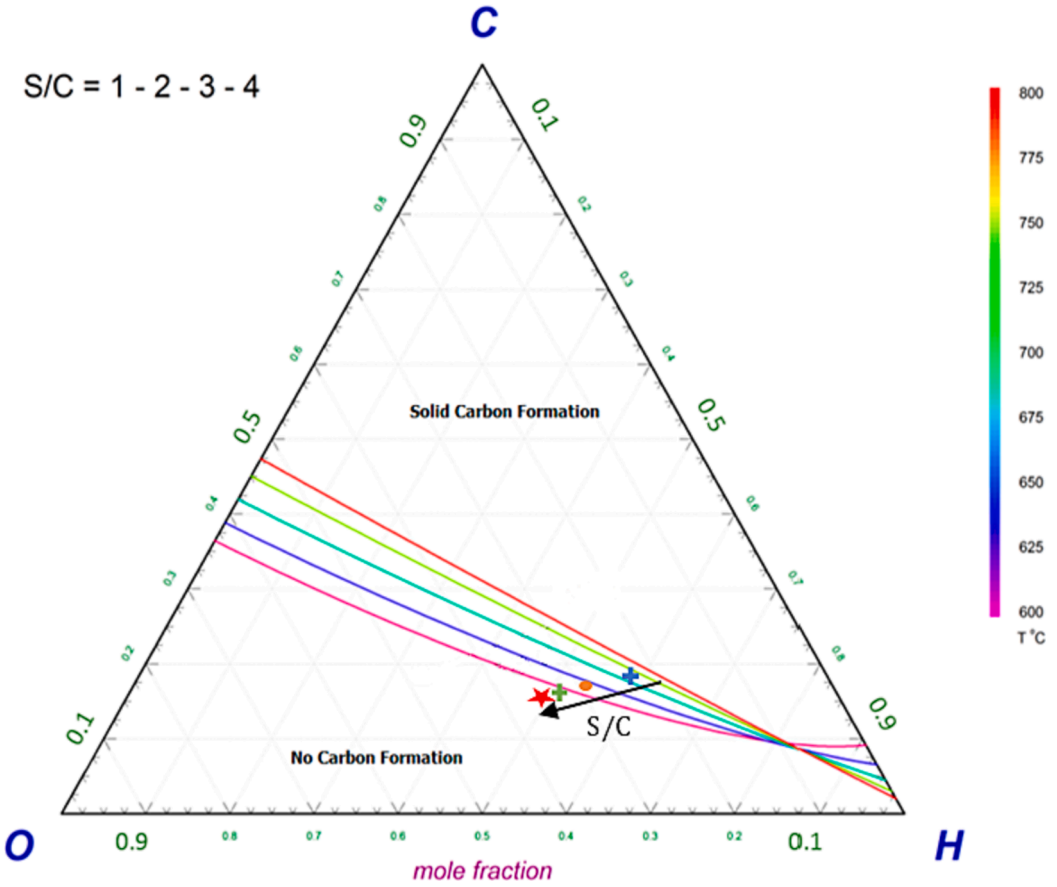

Fig. 16. Ternary C-H-O diagram for the partial oxidation reformer SOFC inlet composition varying the steam to carbon ratio. The orange circle is the base case in which S/C = 2, the blue cross is S/C = 1, the green cross is S/C = 3 and the red star is S/C = 4.

4.4. Solid oxide fuel cell design parameter effect

The effects of changing the SOFC decision variables, including temperature, fuel utilization, operating voltage, and steam-to-carbon ratio, on the electrical and electrical CCS efficiencies of the system were evaluated one at a time. The results, presented in Fig. 15, show the percentage increase or decrease compared to the base-case condition.

Increasing the operating temperature from 800 °C to 900 °C results in an increase in both efficiencies. Conversely, reducing the temperature to 600 °C leads to a decrease in inefficiencies as less methane is converted into reactive molecules (H_2 and CO), resulting in lower current generation and power output. The decreased temperature also causes an increase in the ASR due to higher electrolyte resistance and activation overpotential. Compared to the SOFC operating at 800 °C, the electrical efficiency decreases by around 19 % at 600 °C and gains 0.5 % at 900 °C.

The fuel utilization value also affects the efficiencies. With a fuel utilization of 0.7, both electrical and electrical CCS efficiencies decrease. According to Eq. *(37)*, a decrease in fuel utilization, while maintaining a constant fuel flow rate, leads to a reduction in total current. Simultaneously, under high operating voltage conditions and lower fuel utilization, the current density remains unchanged. Consequently, based on Eq. *(38)*, the number of cells required for the SOFC installation decreases, resulting in a decrease in the electric power generated by the stack- Furthermore, the afterburner requires more oxygen by the ASU increasing the energy consumption. These factors outweigh the energy savings obtained from compressing the air used to remove waste heat.

The operating voltage has a significant impact on the efficiencies. Reducing the operating voltage increases activation and diffusion over

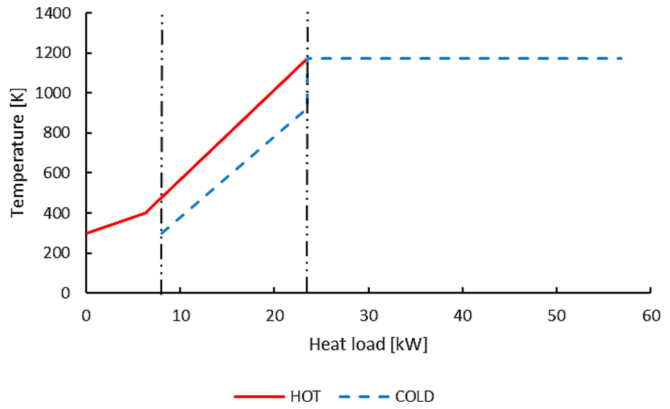

Fig. 17. Calculated results of the Pinch point analysis applied to the energy storage sub-section of the proposed (solar CLMR-SOFC) plant with the corresponding hot (red line) and cold (blue line) composite curves.

potentials but also increases the corresponding current density resulting in a lower ASR. The electric power derived at lower operating voltage decreases but with unchanged values of enthalpy of reaction and internal reforming heat required, the heat that needs to be removed from the cathode air increases (Eq. (43)). This leads to a decrease of 27.4 % and 28.8 % in electrical efficiencies without and with CCS, respectively. On the other hand, higher operating voltages result in lower irreversibility in the stack and higher efficiencies.

Lastly, the steam-to-carbon ratio (S/C) affects methane reforming inside the SOFC. Increasing the S/C ratio leads to higher methane conversion and more power generation. Consequently, both efficiencies gain about three percentage points with S/C = 4 and lose 4 % with S/C = 1.

Another noteworthy observation is that the variation of the first three parameters (temperature, fuel utilization, and operating voltage) does not lead to significant changes in the ternary graph. However, modifying the S/C ratio has a more pronounced effect. Fig. 16 demonstrates that increasing the S/C ratio shifts the system towards a region with no carbonaceous solids formation. This is advantageous as it can help extend the lifespan of the stack by mitigating the formation of carbon deposits.

By maintaining the SOFC temperature at 800 °C and the fuel utilization (FU) factor at 0.85, while adjusting the working voltage from 0.8 to 0.9 and the S/C ratio to 4, the electrical efficiencies without and with CCS reach values of 58.2 % and 56.3 %, respectively.

4.5. Pinch analysis of energy storage island

Pinch analysis was applied to the proposed plant configuration to optimize the heat exchanger network and minimize the external energy requirements. Thermal data from the energy storage section is summarized in Table SM2 with the highest temperature of 1173 K in the reduction reactor and the lowest temperature of 298 K in the storage. The results of the pinch analysis indicate a pinch temperature of 1173 K for the hot stream and 1153 K for the cold stream.

The hot and cold composite curve results are depicted in Fig. 17. A significant amount of heat (8 kW) is available from the hot streams, as shown on the left side of the figure. However, this heat carries low temperatures and is primarily derived from the cooling of syngas compression in the range of 415 K to 298 K. While these heat contents cannot be utilized for internal heating of other cold streams within the plant, they can still be employed for external purposes such as a district heating network (DHN). The central part of the figure represents the heat exchange (15.4 kW) between the hot and cold streams.

The cold stream extends to the right side of the figure, with a maximum temperature of 1173 K and a heat load of 56.8 kW. The difference between the total heat loads (33.4 kW) represents the heating utility provided by concentrated solar power. This high-temperature heat is essential for supporting the endothermic reactions occurring within the reduction reactor.

Table SM3 and Fig. 18 depict the heat exchanger network design and thermal data obtained from the pinch analysis. The reduced ceria particles (PS5) leaving the reduction reactor and flowing into storage R2 contribute 8.4 kW to heat exchanger A, which is connected to the cold methane stream (PS1). The hot solid stream (PS5) heats the methane (PS1) until it reaches 867.2 K. To achieve the desired temperature of 923.15 K, an additional 0.8 kW of heat is required from PS1, which is provided by the syngas (PS4) exiting the reduction reactor and directed to the storage compression train in the heat exchanger B. PS4 then

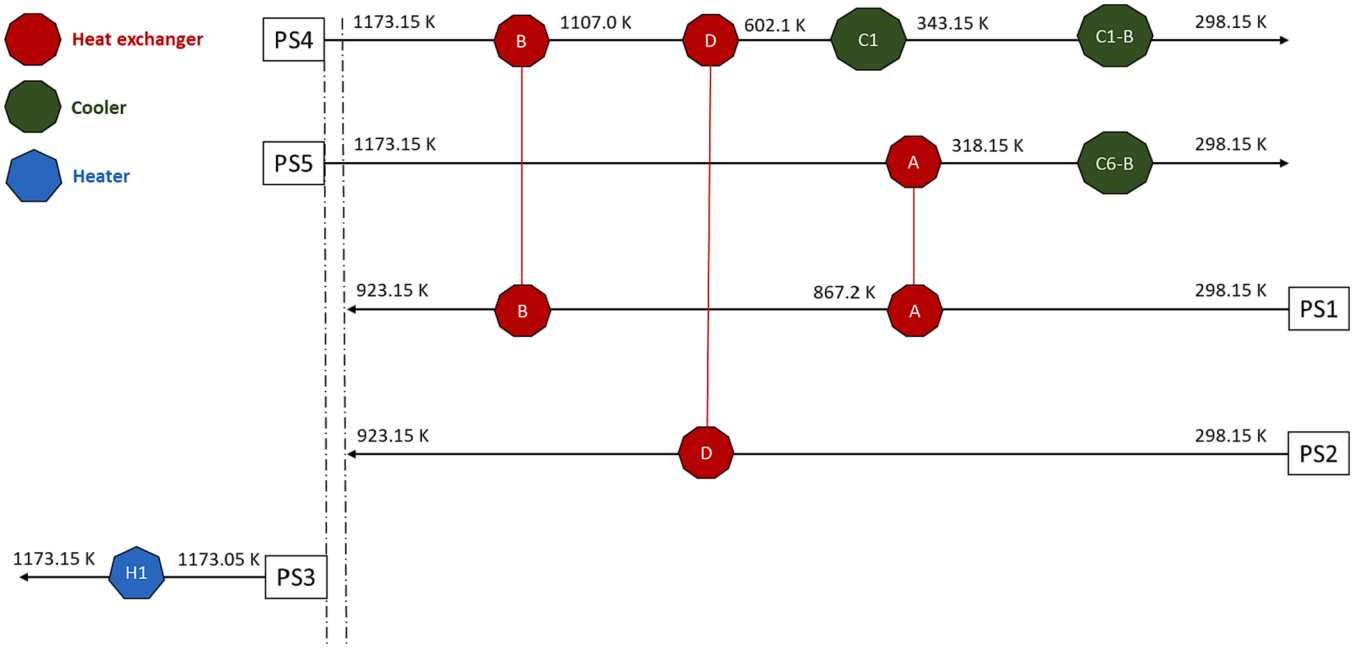

Fig. 18. Heat exchanger network design connecting hot and cold streams of energy storage island for thermal exchange with the focus on minimum external energy consumption for the proposed plant solar CLMR-SOFC.

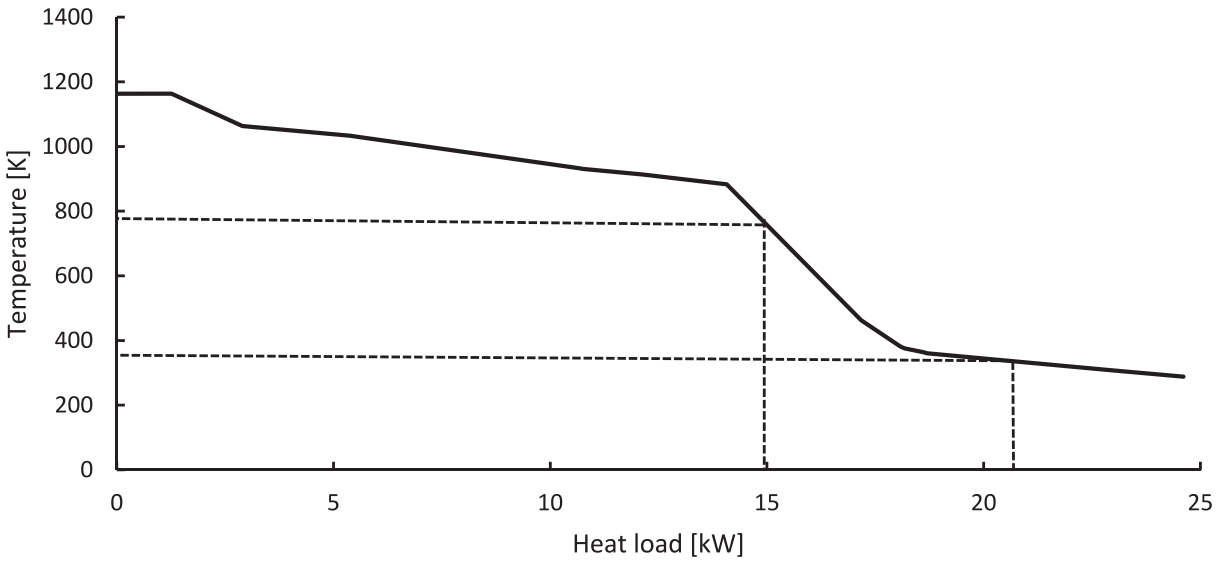

Fig. 19. Grand composite curve resulted from pinch analysis applied to energy release island.

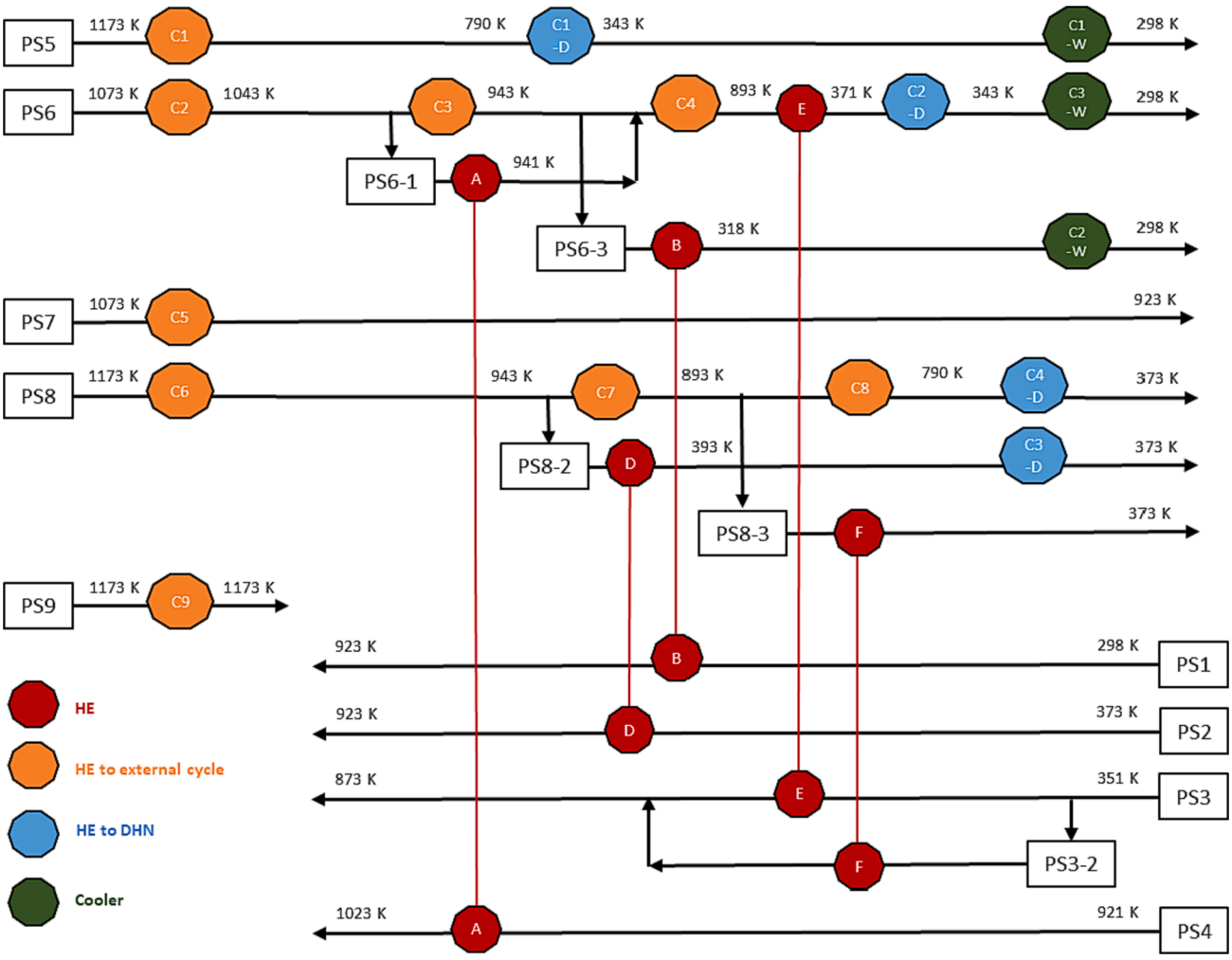

Fig. 20. Heat exchanger network design connecting hot and cold streams of energy release island for thermal exchange. Streams from SP10 to SP14 are not included here for easy representation. They provide part of the heat to the DHN while the other part is lost to the environment.

proceeds to heat exchanger D, where it provides all the required heat (6.3 kW) to the cold ceria (PS2). As a result, the hot syngas is cooled down to 602.1 K and is further utilized in cooler C1 to recover the remaining heat (3.2 kW) for heating water in a district heating network (DHN). Additional coolers (C2, C3, C4, C5) are employed to recover heat from the pressurized syngas (streams 10, 12, 14, and 16). Taking into account cooler C1 as well, approximately 5.55 kW of low-temperature heat can be provided to the DHN. The remaining heat at low temperatures that cannot be recovered amounts to 2.5 kW and is lost to the environment.

4.6. Results of the pinch analysis applied to the energy release section

The energy release island comprises key components such as the oxidation reactor, SOFC, oxy-combustion chamber, and CO_2 train compressors. These components interact through several cold and hot streams, as outlined in Table SM4.

An examination the grand composite curve in Fig. 19 reveals that the plant can meet all its cold stream heat requirements internally, eliminating the need for external heat sources. Additionally, there is a surplus of available heat, totalling 24.6 kW, with a significant portion of it being at temperatures exceeding 800 K. This excess heat can be effectively utilized by an external power cycle to generate additional electricity.

In a previous study [11], optimizations of various s-CO_2 Brayton cycles were carried out, and it was determined that an intercooler s-CO_2 Brayton cycle operating at a turbine inlet temperature of 700 °C achieved an impressive efficiency of 49.4 %. The hot streams could provide 14.8 kW of heat within the temperature range required by the heat transfer fluid for electricity generation (see Table SM5). Consequently, an extra 7.3 kW of electricity could be generated through this process.

For those seeking to maximize the plant's thermal efficiency, even at the cost of a more intricate heat exchanger network, the recovery of low-temperature heat for a district heating network becomes a viable option. Assuming a typical low-temperature network where water enters at 333 K and exits at 363 K, the system can supply approximately 6 kW of heat for district heating purposes. Any remaining heat beyond this requirement would be dissipated to the environment.

The heat exchanger network design for the plant is presented in Fig. 20, and detailed information is provided in Table SM5. In the network, streams SP10 to SP14, which only supply heat at low temperatures to the DHN, are not depicted. The remaining heat from these streams is released into the environment.

To optimize the heat exchanger network, hot streams SP6 and SP8 were divided to provide heat to the cold stream, eliminating the need for a solid–solid heat exchanger. The design involves a total of five heat exchangers for internal plant operations. Additionally, it is possible to install nine additional heat exchangers to provide 14.8 kW of heat to an external power cycle. Furthermore, ten heat exchangers (four of which are represented in the figure) can be included to supply 6 kW of heat to the DHN at low temperatures.

The pinch analysis conducted on the energy release sub-system demonstrates that the plant's heat requirements can be fulfilled internally without the need for external heaters. Moreover, by supplying high-temperature heat to an external power cycle, the electrical efficiency, both without and with CCS, improves by 8.5 %, resulting in values of 65.5 % and 63.6 %, respectively. Furthermore, considering the electricity produced by the external cycle and the provision of hot water to the DHN, the overall efficiency of the system reaches an impressive value of 70 %. This indicates the potential for maximizing the energy utilization and performance of the plant through the integration of the power cycle and DHN.

5. Conclusion

A novel solar CLMR-SOFC process configuration has been proposed for continuous electrical power production, utilizing solar energy storage in the form of syngas and OC particles. This configuration integrates the ceria thermochemical cycle for CO_2 splitting in a methane-driven redox cycle with a SOFC, accompanied by oxyfuel combustion afterburner to mitigate CO_2 emissions. Notably, CO_2 separation is intrinsic to the plant system, with a portion of it being reutilized internally, thereby enhancing the overall efficiency. The proposed plant demonstrates an electrical efficiency surpassing 56.3 %, with a maximum of 63.6 % achievable by utilizing excess high-temperature heat in an external power cycle with complete CO_2 capture. Through rigorous calculations, it has been established that incorporating pinch analysis and DHN optimization in the plant design significantly enhances the global system efficiency by 70 %. Extensive sensitivity analysis has also been conducted to investigate the impact of various plant configurations, such as recirculation of H_2O, CO_2, or a mixture of both into the oxidation reactor, as well as the non-stoichiometric coefficient of the oxygen carrier and key process parameters in the CLMR and SOFC subsystems.

The sensitivity analysis conducted on the proposed plant configuration yielded several significant findings:

- Increasing the fuel reforming ratio (FRR) up to two demonstrated improved performance at the output of the reduction reactor compared to the stoichiometric FRR of 0.5. This increase in methane concentration, limited to a maximum of 50 % at the SOFC inlet, led to an enhanced electrical efficiency with CCS reaching 47.2 % and an energy density of 399 kWh/m^3.
- Exploring the oxidation reactor, different feed compositions were tested, including pure water, pure carbon dioxide, and a combination of both. Notably, feeding the oxidation reactor with pure CO_2 (CSR = 0) resulted in a higher efficiency of 47.5 %, an energy density of 404kWht/m^3 and reduced CO_2 quantity intended for storage, aligning with the principles of the circular economy.
- Gradually reducing the ceria effectiveness parameter (δ) until $\delta = 0.3$ positively impacted the system by leveraging methane internal reforming and increasing overall efficiency. However, further decreasing this parameter would excessively raise the methane concentration entering the SOFC, potentially leading to thermal gradient-induced damage. To mitigate this, reducing the FRR parameter while increasing methane conversion would be sufficient.
- The operating parameters of the SOFC significantly influenced the system's efficiency. Specifically, adjusting the steam-to-carbon ratio (S/C) from 2 to 4 and the operating voltage (V) from 0.8 to 0.9 resulted in a substantial efficiency increase of 8.5 percentage points, reaching a final value of 56.3 %.
- Employing pinch analysis and optimized heat exchanger network (HEN) design in the energy storage and energy release subsections of the plant yielded noteworthy outcomes. The energy storage subsection achieved a minimum energy requirement of 33 kW provided by the sun, along with a thermal gain of 5.5 kW provided to a district heating network (DHN). In the energy release subsection, optimal heat integration was achieved, eliminating the need for external heaters and providing 14.8 kW to an external power cycle and 6 kW to a DHN.
- Overall, the employment of pinch analysis and optimized HEN throughout the entire plant resulted in a thermal gain of 11.5 kW and an electrical gain of 7.3 kW, leading to impressive electricity with CCS efficiency of 63.6 % and a remarkable global efficiency of 70 %.
- Lastly, to the best of the authors' knowledge, this study represents the first comprehensive analysis combining solar CLMR, SOFC, off-gas oxy-combustion, and in-situ CO_2 reutilization, resulting in a 100 % clean energy system with exceptional efficiency.

CRediT authorship contribution statement

Salvatore F. Cannone: . **Muhammad Ishaq:** . **Andrea Lanzini:** Conceptualization, Validation, Writing – review & editing, Supervision.

Massimo Santarelli: Validation, Writing – review & editing, Supervision.

Declaration of competing interest

The authors declare that they have no known competing financial interests or personal relationships that could have appeared to influence the work reported in this paper.

Data availability

Data will be made available on request.

Appendix A. Supplementary data

Supplementary data to this article can be found online at https://doi.org/10.1016/j.enconman.2024.118080.

References

[1] IEA (2022). World Energy Outlook 2022 [Internet]. Paris; 2022 [cited 2023 Oct 20]. Available from: https://www.iea.org/reports/world-energy-outlook-2022.
[2] Michaelides EE. Fossil fuel substitution with renewables for electricity generation – effects on sustainability goals. Eur J Sustainable Dev Res 2019;4(1).
[3] Li D, Xu R, Li X, Li Z, Zhu X, Li K. Chemical looping conversion of gaseous and liquid fuels for chemical production: a review. Energy Fuel 2020;34(5):5381–413.
[4] Warren KJ, Scheffe JR. Kinetic insights into the reduction of ceria facilitated via the partial oxidation of methane. Mater Today Energy 2018;9:39–48.
[5] He YL, Qiu Y, Wang K, Yuan F, Wang WQ, Li MJ, et al. Perspective of concentrating solar power. Energy 2020;198:117373.
[6] Shahabuddin M, Alim MA, Alam T, Mofijur M, Ahmed SF, Perkins G. A critical review on the development and challenges of concentrated solar power technologies. Available from Sustainable Energy Technol Assess [Internet] 2021;47:101434. https://linkinghub.elsevier.com/retrieve/pii/S2213138821004446.
[7] Pelay U, Luo L, Fan Y, Stitou D, Rood M. Thermal energy storage systems for concentrated solar power plants. Renew Sustain Energy Rev 2017;79:82–100.
[8] Ray AK, Rakshit D, Ravikumar K. High-temperature latent thermal storage system for solar power: Materials, concepts, and challenges. Available from Clean Eng Technol [Internet] 2021;4:100155. https://www.sciencedirect.com/science/article/pii/S2666790821001154.
[9] Santamaría Padilla A, Romero-Paredes RH. A thermochemical energy storage materials review based on solid-gas reactions for supercritical CO2 solar tower power plant with a Brayton cycle. J Energy Storage 2023;73:108906.
[10] Cannone SF, Stendardo S, Lanzini A. Solar-powered Rankine cycle assisted by an innovative calcium looping process as energy storage system. Ind Eng Chem Res [Internet]. 2020 Jan 17; Available from:.
[11] Cannone SF, Lanzini A, Stendardo S. An innovative calcium looping process as energy storage system integrated with a solar-powered supercritical CO2 brayton cycle. Frontiers Sustainability 2021;21:2.
[12] Smestad GP, Steinfeld A. Review: photochemical and thermochemical production of solar fuels from H_2O and CO_2 using metal oxide catalysts. Ind Eng Chem Res 2012;51(37):11828–40.
[13] Krenzke PT, Davidson JH. Thermodynamic analysis of syngas production via the solar thermochemical cerium oxide redox cycle with methane-driven reduction. Energy Fuel 2014;28(6):4088–95.
[14] Hong H, Jin H. A novel solar thermal cycle with chemical looping combustion. Int J Green Energy 2005;2(4):397–407.
[15] Jafarian M, Arjomandi M, Nathan GJ. A hybrid solar and chemical looping combustion system for solar thermal energy storage. Appl Energy 2013;103:671–8.
[16] Liu Y, Zhu Q, Zhang T, Yan X, Duan R. Analysis of chemical-looping hydrogen production and power generation system driven by solar energy. Renew Energy 2020;154:863–74.
[17] Tjaden B, Gandiglio M, Lanzini A, Santarelli M, Järvinen M. Small-scale biogas-SOFC plant: technical analysis and assessment of different fuel reforming options. Energy & Fuels [Internet] 2014;28(6):4216–32. https://doi.org/10.1021/ef500212j. Available from:.
[18] Zhou Z, Sun Z, Duan L. Chemical looping: A flexible platform technology for CH4 conversion coupled with CO2 utilization. Curr Opin Green Sustain Chem 2023;39:100721.
[19] Singh S, Bahari MB, Abdullah B, Phuong PTT, Truong QD, Vo DVN, et al. Bi-reforming of methane on Ni/SBA-15 catalyst for syngas production: Influence of feed composition. Int J Hydrogen Energy 2018;43(36):17230–43.
[20] Ma Z, Wang J, Dong F, Han Z, Tian L, Yan R, et al. Thermodynamic analysis of fuel-cell-based combined cooling, heating, and power system integrated solar energy and chemical looping hydrogen generation. Energy 2022;238:121974.
[21] Spallina V, Nocerino P, Romano MC, van Sint AM, Campanari S, Gallucci F. Integration of solid oxide fuel cell (SOFC) and chemical looping combustion (CLC) for ultra-high efficiency power generation and CO2 production. Int J Greenhouse Gas Control 2018;71:9–19.
[22] Zhao H, Zhao Z, Wang H. Thermodynamic performance study of the CLHG/SOFC combined cycle system with CO2 recovery. Energy Convers Manag 2020;223:113319.
[23] Abanades S, Flamant G. Thermochemical hydrogen production from a two-step solar-driven water-splitting cycle based on cerium oxides. Sol Energy 2006;80(12):1611–23.
[24] Shah K, Moghtaderi B, Zanganeh J, Wall T. Integration options for novel chemical looping air separation (ICLAS) process for oxygen production in oxy-fuel coal fired power plants. Fuel 2013;107:356–70.
[25] Abanades S, Haeussler A. Two-step thermochemical cycles using fibrous ceria pellets for H2 production and CO2 reduction in packed-bed solar reactors. Sustain Mater Technol 2021;29:e00328.
[26] Ma Y, Nicholas JD. Mechanical, thermal, and electrochemical properties of Pr doped ceria from wafer curvature measurements. PCCP 2018;20(43):27350–60.
[27] Welte M, Warren K, Scheffe JR, Steinfeld A. Combined ceria reduction and methane reforming in a solar-driven particle-transport reactor. Ind Eng Chem Res 2017;56(37):10300–8.
[28] Chuayboon S, Abanades S, Rodat S. Solar chemical looping reforming of methane combined with isothermal H2O/CO2 splitting using ceria oxygen carrier for syngas production. J Energy Chem 2020;41:60–72.
[29] Ma Z, Martinek J. Analysis of Solar Receiver Performance for Chemical-Looping Integration With a Concentrating Solar Thermal System. J Sol Energy Eng [Internet]. 2019 Jan 8;141(2). Available from: https://doi.org/10.1115/1.4042058.
[30] Zhai R, Li C, Qi J, Yang Y. Thermodynamic analysis of CO2 capture by calcium looping process driven by coal and concentrated solar power. Available from Energy Convers Manag [Internet] 2016;117:251–63. https://www.sciencedirect.com/science/article/pii/S0196890416301534.
[31] National Renewable Energy Laboratory. Partanna MS-LFR CSP Project [Internet]. 2022 [cited 2023 May 9]. Available from: https://solarpaces.nrel.gov/project/partanna-ms-lfr.
[32] JRC Europe commission. PVGIS: Photovoltaic geographical information system [Internet]. JRC- European Commission; 2019 [cited 2023 May 9]. Available from: https://re.jrc.ec.europa.eu/pvg_tools/en/.
[33] van herle J, Maréchal F, Leuenberger S, Favrat D. Energy balance model of a SOFC cogenerator operated with biogas. J Power Sources [Internet]. 2003;118(1):375–83. Available from: https://www.sciencedirect.com/science/article/pii/S0378775303001034.
[34] Chan SH, Khor KA, Xia ZT. A complete polarization model of a solid oxide fuel cell and its sensitivity to the change of cell component thickness. Available from J Power Sources [Internet] 2001;93(1):130–40. https://www.sciencedirect.com/science/article/pii/S0378775300005565.
[35] Wuillemin Z. Experimental and modeling investigations on local performance and local degradation in solid oxide fuel cells. In 2009.
[36] Fuller EN, Schettler PD, Giddings JCalvin. NEW METHOD FOR PREDICTION OF BINARY GAS-PHASE DIFFUSION COEFFICIENTS. Ind Eng Chem [Internet]. 1966 May 1;58(5):18–27. Available from: https://doi.org/10.1021/ie50677a007.
[37] Duan L, Huang K, Zhang X, Yang Y. Comparison study on different SOFC hybrid systems with zero-CO2 emission. Available from Energy [Internet] 2013;58:66–77. https://www.sciencedirect.com/science/article/pii/S0360544213003782.
[38] Yadav S, Mondal SS. A review on the progress and prospects of oxy-fuel carbon capture and sequestration (CCS) technology. Fuel 2022;308:122057.
[39] Hao Q, Zhu L, Wang Y, He Y, Zeng X, Zhu J. Achieving near-zero emission and high-efficient combined cooling, heating and power based on biomass gasification coupled with SOFC hybrid system. Fuel 2024;357:129751.
[40] Cormos CC. Evaluation of energy integration aspects for IGCC-based hydrogen and electricity co-production with carbon capture and storage. Int J Hydrogen Energy 2010;35(14):7485–97.
[41] Rhodes NR, Bobek MM, Allen KM, Hahn DW. Investigation of long term reactive stability of ceria for use in solar thermochemical cycles. Energy 2015;89:924–31.